

# Using electron irradiation to probe iron-based superconductors

Kyuil Cho<sup>1,2</sup> , M Kończykowski<sup>3</sup>, S Teknowijoyo<sup>1,2</sup>, M A Tanatar<sup>1,2</sup>  and R Prozorov<sup>1,2</sup> 

<sup>1</sup> Ames Laboratory, Ames, IA 50011, United States of America

<sup>2</sup> Department of Physics & Astronomy, Iowa State University, Ames, IA 50011, United States of America

<sup>3</sup> Laboratoire des Solides Irradiés, Ecole Polytechnique, CNRS-UMR 7642, CEA, Université Paris-Saclay, F-91128 Palaiseau, France

E-mail: [kcho@ameslab.gov](mailto:kcho@ameslab.gov)

Received 9 January 2018, revised 8 March 2018

Accepted for publication 20 April 2018

Published 14 May 2018



## Abstract

High-energy electron irradiation at low temperatures is an efficient and controlled way to create vacancy–interstitial Frenkel pairs in a crystal lattice, thereby inducing nonmagnetic point-like scattering centers. In combination with London penetration depth and resistivity measurements, the electron irradiation was used as a phase-sensitive probe to study the superconducting order parameter in iron-based superconductors (FeSCs), lending strong support to sign-changing  $s_{\pm}$  pairing. Here, we review the key results of the effect of electron irradiation in FeSCs.

**Keywords:** iron-based superconductors, disorder, electron irradiation, unconventional superconductors, London penetration depth, superconductors

(Some figures may appear in colour only in the online journal)

## 1. Introduction

Due to the unconventional pairing mechanism and relatively high superconducting transition temperatures,  $T_c$ , iron-based superconductors (FeSCs) remain a focus of research activity even a decade after their discovery [1, 2]. A large body of experimental and theoretical works revealed a vast diversity of related compounds unified by multiband superconductivity and proximity to, or direct coexistence with, long-range magnetism. It is impossible to provide a comprehensive list of references here, and we only give some key review articles on basic properties and models [3–33], as well as applications [34–38]. Some of the key contributions come from studies of the effect of controlled disorder induced by the MeV energy range electron irradiation. These relativistic electrons have enough energy to create vacancy–interstitial Frenkel pairs, but not too much energy to induce (undesirable) extended cascades of secondary defects produced by heavier particles, such as protons and  $\alpha$ -particles, or columnar tracks produced by heavy ions of GeV energy [39, 40]. While the superconducting energy gap and critical temperature of an isotropic single-band s-wave superconductor are insensitive to nonmagnetic disorder (Anderson theorem) [41, 42], multiple

gaps, anisotropic gaps, and different gap symmetries are quite sensitive to such disorder, each with a fairly unique response in thermodynamic and transport properties [43–51]. Contrary to the high-temperature cuprates in which a single-gap d-wave superconducting state is firmly established [52], several candidates for pairing symmetry are discussed for FeSCs due to multiple sheets of the Fermi surface supporting nesting and itinerant magnetism [6, 14]. Among them, there are two dominant scenarios for superconducting ‘glue’: spin fluctuations (repulsive interaction), and orbital fluctuations (attractive interaction). The former predicts the state that requires the sign change between different sheets of the Fermi surface ( $s_{\pm}$  pairing) [6], while the latter predicts no sign change ( $s_{++}$  pairing) [45, 46]. Unlike high- $T_c$  cuprates, where phase-sensitive order parameter experiments have a proven d-wave state, similar methods cannot be applied to FeSCs due to the complex multiband electronic band structure. Additional complicated and difficult phase-sensitive techniques (e.g. quasiparticle interference in scanning tunneling microscope measurements) were developed, but they are limited by surface quality and other issues related to tunneling. Alternatives, based on the effects of a controlled nonmagnetic disorder to distinguish  $s_{\pm}$  and  $s_{++}$  pairing states, were

suggested [47, 49] and implemented [39, 40]. Traditionally, the effect of any irradiation on superconductors was assessed by measuring the change of  $T_c$ , critical current, and, sometimes, the upper critical field. This is insufficient since the low-temperature quasiparticles to examine the pairing mechanism need to be studied upon irradiation. Specific heat, thermal conductivity, and London penetration depth are the direct probes that should be used in addition to other measurements. Indeed, electron irradiation combined with London penetration depth measurements was used as an effective phase-sensitive tool to reveal the superconducting gap structure of several FeSCs. For example, the linear temperature dependence of London penetration depth of isovalently substituted  $\text{BaFe}_2(\text{As}_{1-x}\text{P}_x)_2$  changed to an exponential-like dependence using 2.5 MeV electron irradiation, thus suggesting that the nodes are of the accidental type and are lifted upon irradiation [39]. Another example is  $\text{Ba}_{1-x}\text{K}_x\text{Fe}_2\text{As}_2$ , where the evolution of the gap structure was found across the superconducting ‘dome’, particularly near  $x = 0.8$  [40]. In this paper, we summarize the key findings of the effect of electron irradiation in FeSCs. We limit our attention to superconductors derived upon substitution in  $\text{BaFe}_2\text{As}_2$  and  $\text{SrFe}_2\text{As}_2$  (referred in the following as 122 compounds).

## 2. Experimental

### 2.1. Using irradiation to induce structural disorder

Apart from plastic deformation, perhaps the most common way to introduce controlled disorder in solid samples is chemical substitution. Indeed, many such studies were conducted in high- $T_c$  cuprates [53] and FeSCs [29]. However, the substitution changes not only the scattering but also the electronic band structure, chemical potential, lattice parameters, and so on. [29, 53]. The alternative, and technically more involved way, is the irradiation with energetic particles such as heavy ions, protons,  $\alpha$ -particles, neutrons, and electrons. The structure of the resultant disorder depends on the type of irradiation based on the mass, charge, and energy of the particles used [54]. Different types of irradiation should be used to achieve particular goals. For example, some types of heavy-ion irradiation produce columnar defects [55–57], which play very prominent roles in vortex physics of layered materials, but are very difficult to analyze in terms of the scattering centers. Yet early experiments with heavy-ion irradiation in FeSCs have shown a strong violation of the Anderson theorem with saturating behavior of low-temperature London penetration depth, thus providing firm experimental support for multi-band  $s_{\pm}$  pairing [58–60]. Proton [61–64],  $\alpha$ -particle [65], and neutron irradiation were also used in FeSCs. While the results qualitatively indicate multiband pairing, it is hard to achieve quantitative agreement due to the difficulty in analyzing cascades or clusters of defects produced by these types of irradiation. A more detailed systematic investigation of the connection between the size of the defects and  $T_c$  suppression rate was done theoretically in [66].

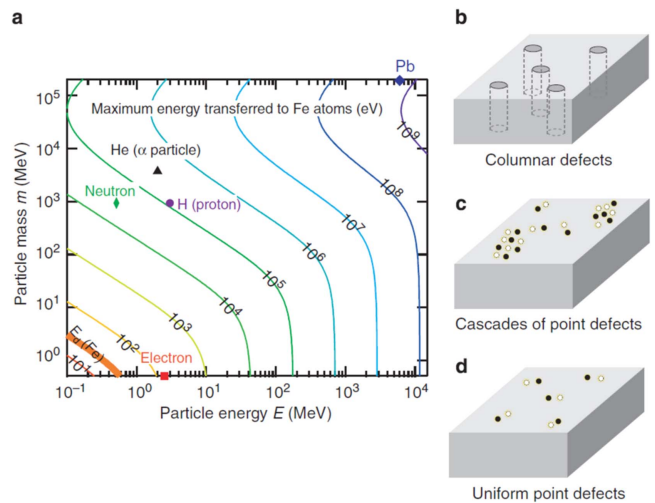


**Figure 1.** (a) Particle energy diagram of various energetic particles used for irradiation. (b)–(d) Different types of defects produced by diverse irradiation techniques. Reprinted with permission from Macmillan Publishers Ltd: Nature Communications [39], Copyright 2014.

Thanks to their small mass and large charge, electrons can be accelerated to relativistic speeds in a highly controlled way using Van der Graaf-type ‘pelletron’ accelerators. The effect of such irradiation on different systems, particularly metals and their compounds, was studied in great detail over more than half a century [54, 67]. Some MeV-range electrons produce point-like defects with minimal impact on the material itself. The large penetration depth of electrons allows homogeneous damage of fairly thick samples (tens of  $\mu\text{m}$ ). Following Mott’s work in 1929 [67], Damask *et al* [54] conducted an analysis of the energy transfer from an accelerated particle smashing into the crystal lattice, and found that only electrons with energies of  $1 \sim 10$  MeV produce point-like defects in the form of interstitial ions and vacancies (Frenkel pairs) that form perfect scattering centers. The energy transferred to an ion due to a head-on collision by a particle of rest mass  $m$  and kinetic energy  $E$  is shown in figure 1. Since the ion displacement energy needed to create a Frenkel pair is typically in the range of 10–50 eV, it is clear from figure 1 that only electrons would produce such individual defects. Higher energy/mass particles lead to secondary impacts resulting in cascades. The interstitials are more mobile and migrate to various ‘sinks’, such as dislocations, grain boundaries, and surfaces, leaving metastable but robust populations of vacancies behind. The studies reviewed in this article were conducted using the 2.5 MeV electron irradiation, which is known to generate point-like disorders in metals and compounds.

### 2.2. Low-temperature electron irradiation

The electron irradiation reviewed in this article was conducted at the SIRIUS facility operated by Laboratoire des Solides Irradiés at École Polytechnique, Palaiseau, France. Its main elements are a pelletron-type accelerator made by the National Electrostatics Corporation (Wisconsin, USA), and a

closed cycle cryo-cooler to maintain liquid hydrogen for cooling the sample. This cooling is required to efficiently channel the heat produced upon collisions between electrons and ions, and to prevent on-site recombination of Frenkel pairs. With a calculated head-on collision displacement energy for Fe ions of 22 eV, and a cross-section to create Frenkel pairs in BaFe<sub>2</sub>As<sub>2</sub> at 2.5 MeV of 115 barn, a dose of 1 C cm<sup>-2</sup> results in about 0.07% of the defects per iron site. Similar numbers were obtained for other ion sites, with cross-sections for Ba and As being 105 and 35 barn, respectively. The electron irradiation was conducted in liquid hydrogen at 22 K, and recombination of the Frenkel pairs upon warming up to room temperature varied depending on compounds; in general, recombination was 20%–30%, as measured directly from the decrease of residual resistivity [68]. After initial annealing, the defects remained stable for most crystals, but some compounds showed gradual slow annealing over months.

### 2.3. Controlled disorder as a phase-sensitive probe

In most previous cases, only the suppression of  $T_c$  with increased disorder was studied. When measurements of  $T_c$  as a function of disorder are combined with measurements of London penetration depth, a phase-sensitive nature of impurity scattering enables distinguishing different scenarios for the superconducting pairing. This combination of measurements was used to identify the accidental character of nodes in isoelectron-substituted BaFe<sub>2</sub>(As<sub>1-x</sub>P<sub>x</sub>)<sub>2</sub> [39] and SrFe<sub>2</sub>(As<sub>1-x</sub>P<sub>x</sub>)<sub>2</sub> [69]. The concomitant suppression of  $T_c$  and closing of gap nodes in the penetration depth study strongly supported  $s_{\pm}$  pairing. More recently, the same idea was used to verify the evolution of a superconducting gap structure in hole-doped Ba<sub>1-x</sub>K<sub>x</sub>Fe<sub>2</sub>As<sub>2</sub> [40].

For unconventional superconductors, one of the important aspects of impurity effects is to mix gaps on different parts of the Fermi surface and thereby smear out the momentum dependence [70]. In the case of a superconducting gap with symmetry-protected nodes, such as a d-wave, this averaging mechanism leads to the suppression of the gap amplitude and the creation of nodal quasiparticles. In penetration depth measurements, this results in crossover from linear temperature-dependent penetration depth  $\Delta\lambda(T)$  in the clean limit to a  $T^2$  dependence in the dirty limit case. In addition to this, the sign change in the order parameter gives rise to impurity-induced Andreev bound states, which lead to additional quasiparticle excitations [71]. Such pair-breaking effects of nonmagnetic impurities have been observed, for example, in Zn-doped YBa<sub>2</sub>Cu<sub>3</sub>O<sub>7</sub> in the bulk measurements of low-temperature penetration depth, where the linear temperature dependence in the clean limit d-wave superconductivity gradually changes to a  $T^2$  dependence with increasing Zn concentrations [72].

It is convenient to characterize the experimental data of low-temperature penetration depth using the power law function  $\Delta\lambda(T) = A + BT^n$ . In the above example of superconductors with symmetry-imposed line nodes, the exponent  $n$  varies with increased disorder in the range between  $n = 1$  (clean limit) and  $n = 2$  (dirty limit). For fully

gapped s-wave superconductors,  $\Delta\lambda(T)$  shows exponential temperature dependence, which can be described as high power law behavior  $n > 3$ , but is  $n = 2$  when it is in the dirty limit.

In sharp contrast, when the nodal positions are not symmetry-protected, as in the nodal s-wave case, the averaging mechanism of impurity scattering can displace the nodes, and at a certain critical impurity concentration the nodes may be lifted if intraband scattering dominates [70], thus eliminating low-energy quasiparticle excitations. In power law analysis of the penetration depth data, this crossover would lead to exponent  $n$  acquiring values  $n > 2$ . In the fully gapped state after lifting the node, we have two cases in multiband superconductors. If the signs of the order parameter on different bands are opposite, residual interband scattering can give rise to midgap Andreev bound states localized at nonmagnetic impurities that can contribute to low-energy excitations, provided that the concentration of impurities is sufficient to create such states. If there is no sign change, the gap and  $T_c$  will be independent of disorder at some high-rate impurity/defect scattering: since no Andreev states will be created, no significant change in low-energy excitations is expected. Indeed, such a difference between nodal sign-changing  $s_{\pm}$  and sign-preserving  $s_{++}$  cases has been theoretically suggested by the recent calculations for multiband superconductivity, considering the band structure of FeSCs [49]. Therefore, studying the effect of impurity/defects on the gap nodes and low-energy excitations can be used as a powerful probe for the pairing symmetry of superconductors.

### 2.4. London penetration depth

The London penetration depth of FeSCs has been measured using a variety of techniques, such as muon-spin rotation [73–75], frequency-dependent conductivity [76, 77], microwave cavity perturbation [78–80], mutual inductance [81], magnetic force and superconducting quantum interference device microscopy [82, 83], measurements of the first critical field using either global [84, 85] or local probes [86, 87], nitrogen-vacancy center in diamond magnetometry [88], and the self-oscillating tunnel diode resonator (TDR) [84, 89–91]. There are pros and cons for each method. The most important advantage of the TDR technique is that it provides the highest resolution of London penetration depth: sub-Å for a sub-mm size sample. Since the technical details are available in previous review articles [92–94], here we only briefly describe some of the key aspects of this technique.

The TDR is a self-oscillating tank circuit that resonates at its fundamental frequency ( $f_0 = \frac{1}{2\pi\sqrt{L_0C}}$ ). In Ames Laboratory and other research labs, researchers were able to make a TDR circuit ( $f_0 \cong 14$  MHz) with high stability of 1 part per  $10^9$  [93]. When a nonmagnetic conducting sample is inserted into a TDR coil, it induces a change in frequency ( $\Delta f$ ). In the case of a finite-size sample with magnetic susceptibility ( $\chi$ ),

#### D. London penetration depth

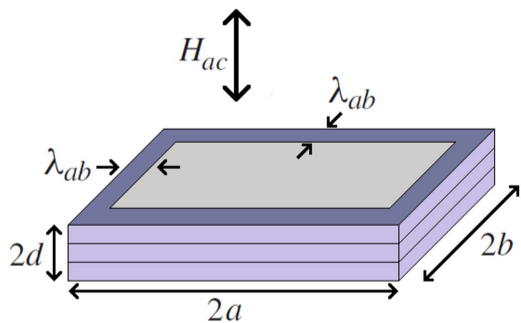


**Figure 2.** Typical sample dimensions for measurements of in-plane penetration depth  $\lambda_{ab}$ .  $2a \times 2b \times 2d \approx 500 \mu\text{m} \times 500 \mu\text{m} \times 50 \mu\text{m}$ . The ac magnetic field of  $H_{ac}$  ( $\sim 20$  mOe) is produced by the TDR coil.

the frequency change can be described as

$$\Delta f = -\frac{f_0 V_s}{2 V_c} 4\pi \chi, \quad (1)$$

where  $V_s$  and  $V_c$  are the volumes of the sample and TDR coil, respectively. For a finite-size sample of rectangular slab, the magnetic susceptibility ( $\chi$ ) can be written as

$$-4\pi\chi = \frac{1}{1-N} \left[ 1 - \frac{\lambda_{ab}}{R} \tanh\left(\frac{R}{\lambda_{ab}}\right) \right], \quad (2)$$

$$\approx \frac{1}{1-N} \left[ 1 - \frac{\lambda_{ab}}{R} \right], \text{ if } R \gg \lambda_{ab}. \quad (3)$$

Here,  $R$  is the effective dimension, and  $N$  is a demagnetization factor. For a rectangular slab with dimensions of  $2a \times 2b \times 2d$  (figure 2),  $R$  can be approximated as in [94],

$$R \approx \frac{\omega}{2 \left[ 1 + \left( 1 + \left( \frac{2d}{\omega} \right)^2 \right) \arctan\left(\frac{\omega}{2d}\right) - \frac{2d}{\omega} \right]}, \quad (4)$$

with  $\omega \approx \frac{2ab}{a+b}$ . Combining equations (1) and (3), the relation between  $\Delta f$  and  $\lambda_{ab}$  is obtained as follows:

$$\Delta f = \frac{f_0 V_s}{2 V_c} \frac{1}{1-N} \left[ 1 - \frac{\lambda_{ab}}{R} \right], \quad (5)$$

$$= G \left[ 1 - \frac{\lambda_{ab}}{R} \right], \quad (6)$$

where  $G$  ( $= \frac{f_0 V_s}{2 V_c} \frac{1}{1-N}$ ) is a geometric calibration constant that can be directly measured by pulling the sample out of the coil. Thus, the variation of penetration depth ( $\delta\lambda_{ab}$ ) from  $T_{\min}$  to  $T$  is

$$\delta\lambda_{ab} = \lambda_{ab}(T) - \lambda_{ab}(T_{\min}), \quad (7)$$

$$= \frac{R}{G} (\Delta f(T_{\min}) - \Delta f(T)). \quad (8)$$

Based on equation (8), one can measure the change in London penetration depth ( $\delta\lambda_{ab}$ ) from the change in the frequency. When a sub-mm scale sample is used, one part per billion resolution in a TDR frequency can be converted to sub-Å resolution in  $\lambda_{ab}$ .

### 3. Effect of electron irradiation on the 122 compounds

#### 3.1. Materials

The FeSCs in the 122 family share several common characteristics. One of them is the ubiquitous appearance of superconductivity with the highest  $T_c$  near the edge of the domain of long-range magnetic ordering in the phase diagram, regardless of the types of chemical substitution. As an example, figure 3 shows phase diagrams of various 122 FeSCs: hole-doped  $\text{Ba}_{1-x}\text{K}_x\text{Fe}_2\text{As}_2$  [95]; isovalently doped  $\text{BaFe}_2(\text{As}_{1-x}\text{P}_x)_2$  [96],  $\text{Ba}(\text{Fe}_{1-x}\text{Ru}_x)_2\text{As}_2$  [97], and  $\text{SrFe}_2(\text{As}_{1-x}\text{P}_x)_2$  [98]; and electron-doped  $\text{Ba}(\text{Fe}_{1-x}\text{Co}_x)_2\text{As}_2$  [99] and  $\text{Ba}(\text{Fe}_{2-x}\text{Ni}_x)\text{As}_2$  [100]. In all cases, the superconducting dome occurs with the suppression of the magnetic phase, and the maximum  $T_c$  is located where the anti-ferromagnetic order is expected to disappear. Gradual suppression of the magnetic order with composition as a tuning parameter [101] suggests the existence of the quantum critical point, and thus the close relation between magnetic fluctuations and the maximum  $T_c$ . The most clear case for the quantum critical scenario is found in isovalently substituted  $\text{BaFe}_2(\text{As}_{1-x}\text{P}_x)_2$ , for which both in-plane and inter-plane resistivities show linear temperature dependence at optimal doping [102] (see the middle panel in the right column of figure 4). Indeed, the quantum critical point is observed beneath the superconducting dome in  $\text{BaFe}_2(\text{As}_{1-x}\text{P}_x)_2$  by measuring the zero-temperature penetration depth [96].

However, several important differences are observed depending on the type of chemical substitutions in both normal and superconducting states. For example, the temperature-dependent resistivity shows quite distinct behavior as shown in figures 4 and 5. Another significant difference comes from distinct superconducting gap order parameters. While similar Fermi surfaces are found among different types of substitutions, the superconducting gap structures vary from nodal gaps in  $\text{BaFe}_2(\text{As}_{1-x}\text{P}_x)_2$  [96] to anisotropic gaps in  $\text{Ba}(\text{Fe}_{1-x}\text{Co}_x)_2\text{As}_2$  [103]. More interestingly, the order parameter of  $(\text{Ba}_{1-x}\text{K}_x)\text{Fe}_2\text{As}_2$  [40] is known to evolve with doping from a full gap ( $x < 0.8$ ) to a gap with accidental nodes for compositions  $x > 0.8$ , due to the Lifshitz transition in Fermi surfaces [104, 105]. In this section, we will review the effect of electron irradiation on six 122 FeSCs: hole-doped  $\text{Ba}_{1-x}\text{K}_x\text{Fe}_2\text{As}_2$ ; isovalently doped  $\text{BaFe}_2(\text{As}_{1-x}\text{P}_x)_2$ ,  $\text{Ba}(\text{Fe}_{1-x}\text{Ru}_x)_2\text{As}_2$ , and  $\text{SrFe}_2(\text{As}_{1-x}\text{P}_x)_2$ ; and electron-doped  $\text{Ba}(\text{Fe}_{1-x}\text{Co}_x)_2\text{As}_2$  and  $\text{Ba}(\text{Fe}_{2-x}\text{Ni}_x)\text{As}_2$ .

#### 3.2. Hole-doped $\text{Ba}_{1-x}\text{K}_x\text{Fe}_2\text{As}_2$

$(\text{Ba}_{1-x}\text{K}_x)\text{Fe}_2\text{As}_2$  is one of the most intensively studied compounds among FeSCs due to the evolution of its superconducting gap structure over compositions ( $x$ ). In the optimally doped region ( $x = 0.35\text{--}0.4$ ), two effective isotropic superconducting gaps were identified in various experiments, such as thermal conductivity [108], London penetration depth [109, 110], and angle-resolved photoemission spectroscopy (ARPES) [110, 111–113]. However, a gap with line nodes

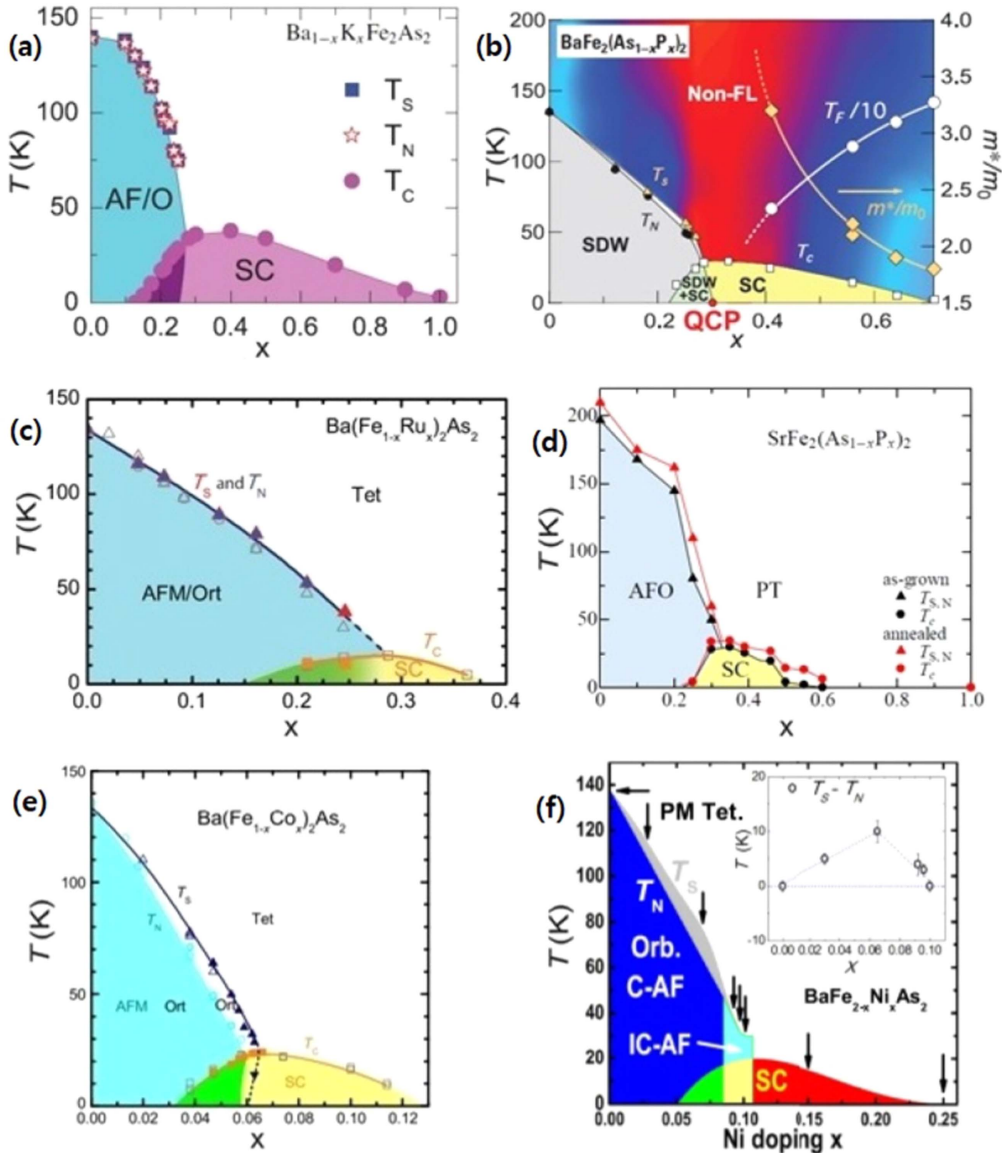


**Figure 3.** Phase diagrams of 122 family of FeSCs: (a) hole-doped  $\text{Ba}_{1-x}\text{K}_x\text{Fe}_2\text{As}_2$  [95]; (b) isovalently doped  $\text{BaFe}_2(\text{As}_{1-x}\text{P}_x)_2$  [96], (c)  $\text{Ba}(\text{Fe}_{1-x}\text{Ru}_x)_2\text{As}_2$  [97], and (d)  $\text{SrFe}_2(\text{As}_{1-x}\text{P}_x)_2$  [98]; and (e) electron-doped  $\text{Ba}(\text{Fe}_{1-x}\text{Co}_x)_2\text{As}_2$  [99] and (f)  $\text{Ba}(\text{Fe}_{2-x}\text{Ni}_x)\text{As}_2$  [100]. Panels (a), (c), (e), and (f): reprinted figures with permission from [95, 97, 99, 100], Copyright 2012, 2011, 2010 and 2015 by the American Physical Society. Panel (b): from [96]. Reprinted with permission from AAAS. Panel (d): reproduced with permission from [98].

was identified in the heavily overdoped region ( $x \geq 0.8$ ) from thermal conductivity [114–117], London penetration depth [118], and ARPES [111, 113]. This dramatic change in the superconducting gap structure is likely to be connected to the Lifshitz transition near  $x = 0.7$ –0.9, where the electron-like pockets at the M point changes to hole-like pockets [104, 105]. The evolution of the gap structure has been discussed in several models: (i) a crossover between two generalized s-wave states, where the usual configuration of isotropic gaps with opposite signs on the electron and hole pockets crosses over to a configuration with opposite signs on the hole pockets, and resulting in accidental nodes [117]; (ii) an intermediate time-reversal symmetry-broken  $s + is$  state [119]; (iii) a transition from  $s_{\pm}$  to d-wave either directly [120] or with an intermediate  $s + id$  state [14, 121, 122]; and

(iv) the existence of too-small-to-measure but finite ‘Lilliputian’ gaps [123, 124].

To resolve this unusual variation, the 2.5 MeV electron irradiation in combination with resistivity and London penetration depth measurements was used by Cho *et al* [40, 109]. First of all, the electron irradiation effectively suppresses  $T_c$  over all compositions, as shown in figure 6. The large suppression of  $T_c$  occurs in both underdoped and overdoped compositions. For underdoped compositions (figure 7(a)), the magnetic transition temperature  $T_N$  (or  $T_{SM}$ ) is also effectively suppressed in  $x = 0.19$ . Interestingly, the decrease of  $\Delta T_c = -4.8$  K is comparable to  $\Delta T_N = -5.1$  K (figure 7(a)). This correlation between  $\Delta T_c$  and  $\Delta T_N$  also exists in another underdoped composition of  $x = 0.22$ , as shown in figure 9(b). One can test if this correlation exists in

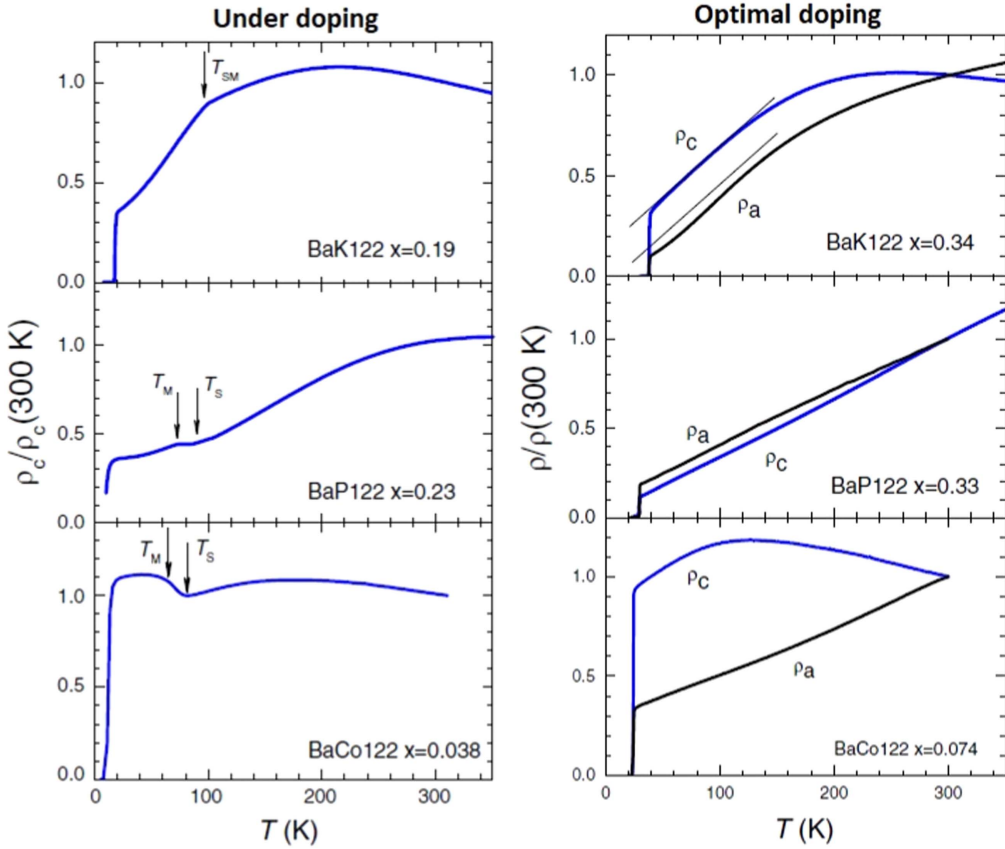


**Figure 4.** Temperature-dependent resistivity of underdoped and nearly optimally doped representative 122 FeSCs:  $(\text{Ba}_{1-x}\text{K}_x)\text{Fe}_2\text{As}_2$ ,  $\text{BaFe}_2(\text{As}_{1-x}\text{P}_x)_2$ , and  $\text{Ba}(\text{Fe}_{1-x}\text{Co}_x)_2\text{As}_2$ . Reprinted figure with permission from [102], Copyright 2014 by the American Physical Society.

isovalently doped  $\text{BaFe}_2(\text{As}_{1-x}\text{P}_x)_2$ , as will be shown later in figure 20; however, there exists no particular correlation potentially due to the influence of the quantum critical point. For further analysis of  $T_c$  suppression in  $\text{Ba}_{1-x}\text{K}_x\text{Fe}_2\text{As}_2$ , the changes in  $T_c$  and normalized  $T_c$  upon irradiation are summarized in figure 8. This figure clearly shows that heavily underdoped and overdoped samples are most susceptible against irradiation.

Since the effect of irradiation varies in different materials, the dosage is not a good parameter to indicate the amount of disorder. To avoid this problem we used an increase of the normal state residual resistivity upon irradiation as a measure of disorder, which is clearly seen in figure 7. Figure 11(a) summarizes  $\Delta t_c = \Delta T_c/T_{c0}$  as a function of  $\Delta\rho$ .

Experimentally determined values of resistivity increase ( $\Delta\rho$ ) and the absolute value of London penetration depth ( $\lambda_0$ ) enable us to define the dimensionless scattering rate as [68, 126]

$$g^\lambda = \frac{\hbar\Delta\rho}{2\pi k_B\mu_0 T_{c0} \lambda_0^2}, \quad (9)$$

where  $\lambda_0$  is the zero-temperature London penetration depth,  $T_{c0}$  is  $T_c$  before irradiation, and  $\Delta\rho$  is the variation of residual resistivity. The relative change in superconducting transition temperature  $\Delta t_c = \Delta T_c/T_{c0}$  as a function of resistivity change  $\Delta\rho$  is summarized in figure 11(a). The values of  $\lambda_0$  available from the literature [127, 110, 128, 129] are plotted

in figure 10. Since there are no reports on  $\lambda_0$  in the overdoped region, we only consider compositions with  $x \leq 0.6$ . Based on these parameters, the variation of reduced transition temperature  $t_c = T_c/T_{c0}$  is calculated as a function of dimensionless parameter ( $g^\lambda$ ), as shown in figure 11(b). In general,  $t_c$  shows a substantial decrease with increasing  $g^\lambda$ , but much slower than the Abrikosov–Gor’kov value.

The London penetration depth was also measured for all compositions upon increasing dose of irradiation, as shown in figure 12. In the optimally doped region, the exponent of the power law fit  $n$  (bottom panel) is above 4, which is experimentally indistinguishable from exponential dependence. This is a clear signature of the full gap superconductivity. However, upon moving away from the optimal doping, the exponent decreases toward  $n = 2$  for the underdoped region and below  $n = 2$  for the overdoped region. The former finding is consistent with a previous study on strongly underdoped compositions [130], and is interpreted as anisotropy appearing due to coexistent magnetic order [131]. The linear temperature behavior of low-temperature penetration depth in the overdoped region is a signature of nodal gaps. To understand this doping-dependent variation of the superconducting gap structure, a minimal two-gap model is introduced to fit the penetration depths of all pristine samples (see the supplementary materials of [40] for details).

$$\Delta_l = \Delta_{0l}(1.0 + r_l \cos 4\phi) \quad (10)$$

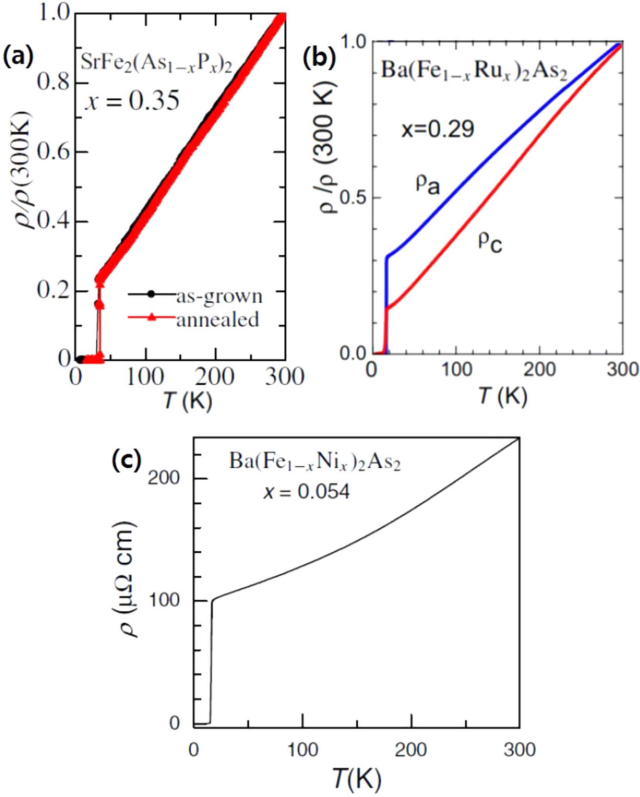


**Figure 5.** Temperature-dependent resistivity of nearly optimally doped 122 FeSCs:  $\text{SrFe}_2(\text{As}_{1-x}\text{P}_x)_2$  [98],  $\text{Ba}(\text{Fe}_{1-x}\text{Ru}_x)_2\text{As}_2$  [106], and  $\text{Ba}(\text{Fe}_{1-x}\text{Ni}_x)_2\text{As}_2$  [107]. Panel (a): reprinted with permission from [98]. Panels (b) and (c): reprinted with permission from [106, 107], Copyright 2014 and 2013 by the American Physical Society.

$$\Delta_2 = \Delta_{02}(1.0 + r_2 \cos 4\phi) \quad (11)$$

Then, the interaction potentials were calculated, and the impurity scattering upon electron irradiation was treated within a self-consistent  $t$ -matrix approximation. Considering the Fermi surface change near the Lifshitz transition at  $x \sim 0.8$  (figure 13), all results of penetration depth were fitted with this model, and the superconducting gap evolution was found as shown in figure 14. Interestingly, all experimental data are well explained assuming that the sign change between hole and electron pockets (near the optimally doped region) varies compared to the sign change within the same hole pockets in the heavily overdoped region. This clearly supports that the nodes observed in  $x > 0.8$  are not symmetry-imposed, but are accidental nodes, which is consistent with various other experimental observations.

### 3.3. Isovalent-substituted $\text{BaFe}_2(\text{As}_{1-x}\text{P}_x)_2$

$\text{BaFe}_2(\text{As}_{1-x}\text{P}_x)_2$  is an isovalently substituted FeSC that has a maximum  $T_c \sim 30$  K [132]. This compound is particularly interesting due to the presence of a quantum critical point beneath the superconducting dome, as shown in figure 3(b) [96], and nodal superconducting gaps over all compositions [23]. Since the nodes can be symmetry-imposed (as in the d-wave case) or accidental, the origin of the nodal gap structure in  $\text{BaFe}_2(\text{As}_{1-x}\text{P}_x)_2$  has been a key research question. This question was answered by conducting a combined study of

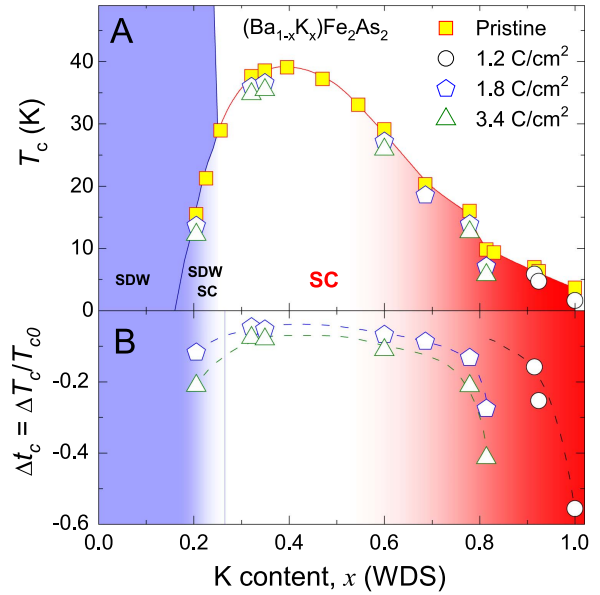


**Figure 6.** (A)  $T_c$  versus  $x$  phase diagram of pristine (squares) and electron-irradiated (other symbols, see legend) samples. SDW, spin-density wave; SC, superconducting phase. (B) Normalized suppression of  $T_c$  ( $\Delta T_c = \Delta T_c/T_{c0}$ ) versus  $x$ . Adapted from [40]. © The Authors, some rights reserved; exclusive licensee American Association for the Advancement of Science. Distributed under a Creative Commons Attribution Non-Commercial License 4.0 (CC BY-NC).

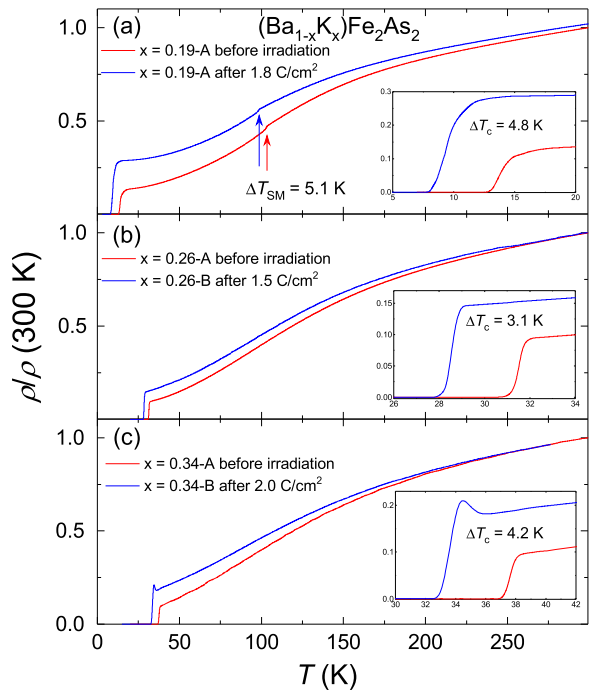


**Figure 7.** Evolution of the temperature-dependent resistivity (normalized by the value at 300 K) upon electron irradiation in  $\text{Ba}_{1-x}\text{K}_x\text{Fe}_2\text{As}_2$ : (a)  $x = 0.19$ , (b)  $x = 0.26$ , and (c)  $x = 0.34$ . Reprinted figure with permission from [109], Copyright 2014 by the American Physical Society.

electron irradiation and measurement of low-temperature penetration depth by Mizukami *et al* [39]. As shown in figure 15, the electron irradiation effectively suppresses  $T_c$  down to 0.44  $T_{c0}$ . Simultaneously, the low-temperature

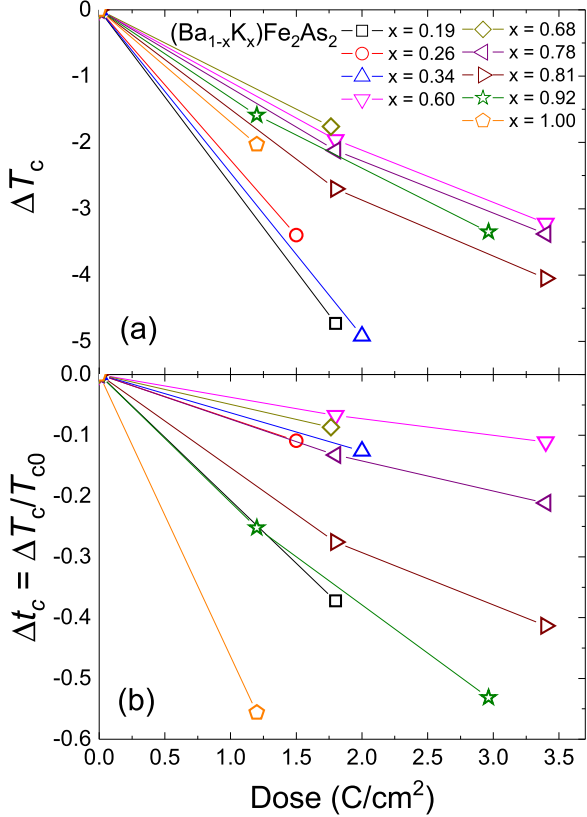


**Figure 8.**  $T_c$  suppression in  $\text{Ba}_{1-x}\text{K}_x\text{Fe}_2\text{As}_2$  upon electron irradiation: (a)  $\Delta T_c$  and (b)  $\Delta t_c = \Delta T_c/T_{c0}$  versus irradiation dose. Data from [40, 109].

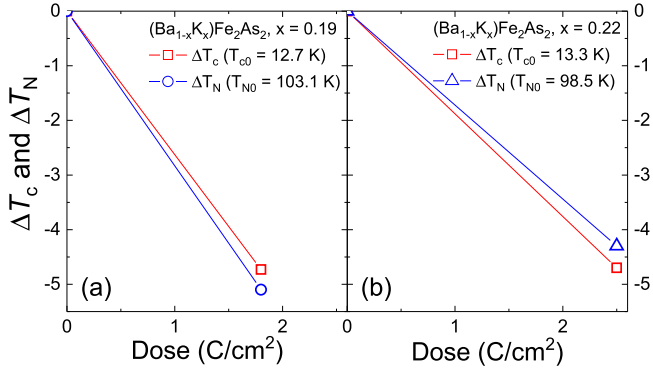


**Figure 9.** Comparison between  $\Delta T_c$  and  $\Delta T_N$  upon electron irradiation for  $x = 0.19$  [109] and  $0.22$  [125] of  $\text{Ba}_{1-x}\text{K}_x\text{Fe}_2\text{As}_2$ .

penetration depth shows a non-monotonic evolution of the power law exponent  $n$ , from  $n \sim 1$  ( $T$  linear) to above  $n > 3$  (exponential), and then back to  $n \sim 2$  ( $T^2$ ). If the nodes in the gap were symmetry-imposed, the monotonic change from linear  $T$  to  $T^2$  with disorder should be expected. Thus, the occurrence of exponential penetration depth during the irradiation clearly supports the presence of accidental nodes [39]. Furthermore, Mizukami *et al* [133] carefully investigated how the superconducting dome changes upon irradiation, and found the superconducting dome shift toward the lower composition side, as shown in figure 16. This implies that the maximum  $T_c$  follows the location of the quantum critical point because it also moves toward lower  $x$ .

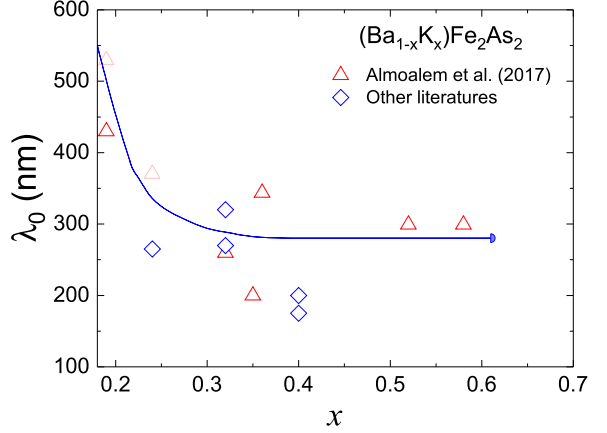


**Figure 10.** Zero-temperature penetration depth ( $\lambda_0$ ) of  $\text{Ba}_{1-x}\text{K}_x\text{Fe}_2\text{As}_2$  from [127, 110, 128, 129].

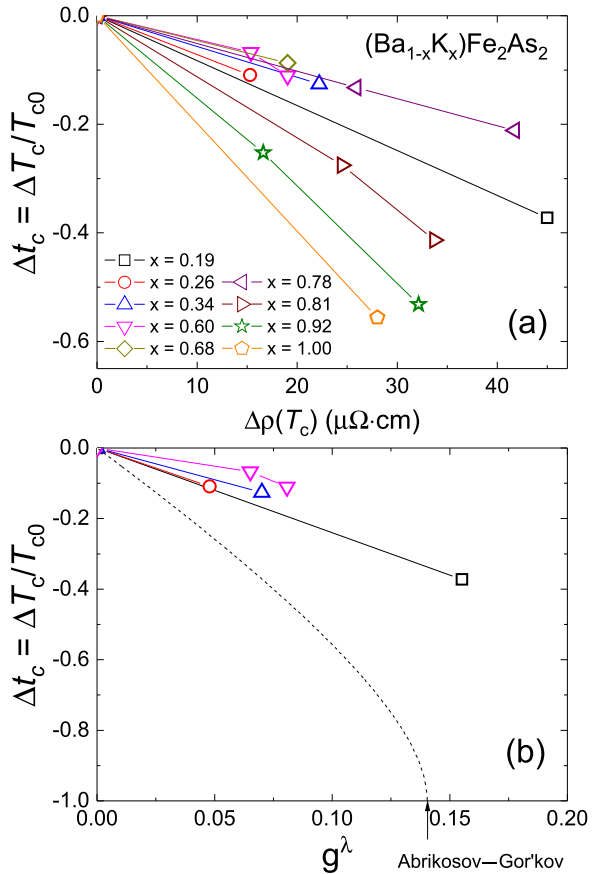


**Figure 11.** Normalized suppression  $t_c (= \Delta T_c/T_{c0})$  as functions of (a)  $\Delta\rho$  and (b)  $g^\lambda$ .  $g^\lambda$  is calculated only for  $x < 0.6$ , where experimental  $\lambda_0$  is available from the literature.

To characterize  $T_c$  suppression more quantitatively, we calculate the dimensionless scattering parameter ( $g^\lambda$ ). For this purpose, we summarize the zero-temperature London penetration depth of  $\text{BaFe}_2(\text{As}_{1-x}\text{P}_x)_2$  from the literature in figure 17(b), and the  $T_c$  versus dose of electron irradiation in figure 18. At the optimally doped region ( $x = 0.30$  and  $0.33$ ), large doses of electron irradiation were applied up to  $11.2$  and  $15.5 \text{ C cm}^{-2}$ , respectively. For both compositions,  $T_c$  drops linearly without any sign of saturation. This is strong

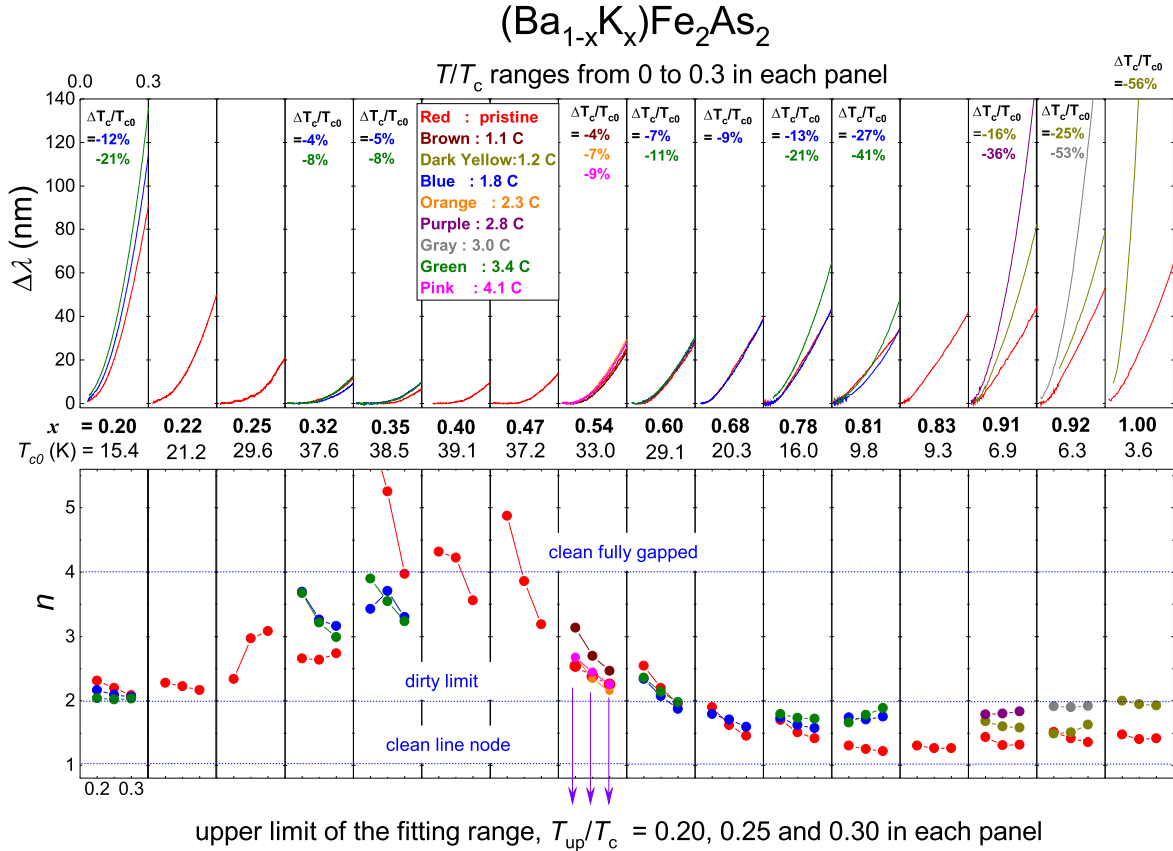


**Figure 12.** Evolution of temperature dependence of London penetration depth ( $\Delta\lambda$ ). Upper panels:  $\Delta\lambda$  versus  $T/T_c$  for 16 different compositions before and after electron irradiation. Each individual panel shows a low-temperature region of  $T/T_c < 0.3$  (full-range curves are shown in figure S1 of [40]). Lower panels: exponent  $n$  obtained from the power law fitting,  $\Delta\lambda = A(T/T_c)^n$ . For each curve, three different upper-limit temperatures were used,  $T_{up}/T_c = 0.20, 0.25$ , and  $0.30$ , whereas the lower limit was fixed by the lowest temperature. Adapted from [40]. © The Authors, some rights reserved; exclusive licensee American Association for the Advancement of Science. Distributed under a Creative Commons Attribution Non-Commercial License 4.0 (CC BY-NC).

evidence against  $s_{++}$  pairing, but is consistent with sign-changing  $s_{\pm}$  pairing. Among the data in figure 18, only limited data have corresponding resistivity  $\Delta\rho$  upon irradiation. For those data,  $\Delta T_c = \Delta T_c/T_{c0}$  versus  $\Delta\rho$  is plotted in figure 19(a). Following equation (9), the dimensionless parameter is calculated and plotted in figure 19(b). In general, the suppression of  $t_c$  is similar among different compositions. More interestingly, these values are very close to the Abrikosov-Gor'kov value. Another interesting fact is shown in figure 20, where the suppression rates of  $\Delta T_N$  of underdoped compositions ( $x = 0, 0.16, 0.24, 0.28$ ) are very similar. The reason for these similar suppression rates requires further studies. Unlike hole-doped  $\text{Ba}_{1-x}\text{K}_x\text{Fe}_2\text{As}_2$ ,  $\Delta T_c$  is not comparable to  $\Delta T_N$ , potentially due to the presence and shift of the quantum criticality point.

### 3.4. Isovalently substituted $\text{Ba}(\text{Fe}_{1-x}\text{Ru}_x)_2\text{As}_2$

Similar to other substitutions in 122 FeSCs, isovalent ruthenium substitution on the iron site of  $\text{BaFe}_2\text{As}_2$  also suppresses long-range magnetic order and induces superconductivity with range of bulk coexistence, see composition phase diagram in figure 3(c). Unlike in electron-doped FeSCs, the structural and magnetic transitions remain coincident in

temperature. The compensation condition between hole and electron carriers does not change in this compound [135–138]. Since the quantum critical point was discovered in nodal gap superconductor  $\text{BaFe}_2(\text{As}_{1-x}\text{P}_x)_2$ , it is interesting to see the effect of Ru-substitution as another isovalently substituted compound.

Prozorov *et al* [68] conducted *in situ* and *ex situ* measurements of the resistivity in a slightly underdoped single crystal of  $\text{Ba}(\text{Fe}_{1-x}\text{Ru}_x)_2\text{As}_2$  ( $x = 0.24$ ) with an increasing dose of 2.5 MeV electron irradiation, as shown in figure 21. The suppression of  $T_c$  is summarized in figure 22. Furthermore, the dimensionless scattering rate  $g^\lambda$  is calculated following equation (9), and is plotted in figure 23. In general, a rapid suppression of  $T_c$  is observed, which cannot be explained by the  $s_{++}$  scenario, but supports the  $s_{\pm}$  pairing mechanism. The rate of suppression is much slower than that of  $\text{BaFe}_2(\text{As}_{1-x}\text{P}_x)_2$ .

### 3.5. $\text{SrFe}_2(\text{As}_{1-x}\text{P}_x)_2$

The phase diagram of another 122 compound with isovalent substitution,  $\text{SrFe}_2(\text{As}_{1-x}\text{P}_x)_2$ , with the maximum value of  $T_c \sim 30$  K, is very similar to that of  $\text{BaFe}_2(\text{As}_{1-x}\text{P}_x)_2$  (figure 3(d)). In particular, it also shows nodal superconducting gaps [139, 140]. Specific heat and nuclear magnetic resonance

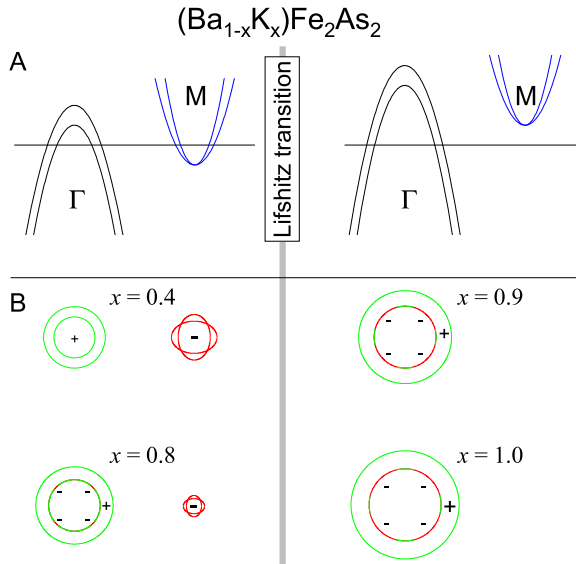


**Figure 13.** (a) Schematic change in the electronic band structure across the Lifshitz transition. (b) Hole ( $\Gamma$ ) and electron (M) pockets relevant for calculations with the sign-changing order parameter. Signs are encoded by green (+) and red (−) colors. Adapted from [40]. © The Authors, some rights reserved; exclusive licensee American Association for the Advancement of Science. Distributed under a Creative Commons Attribution Non-Commercial License 4.0 (CC BY-NC).

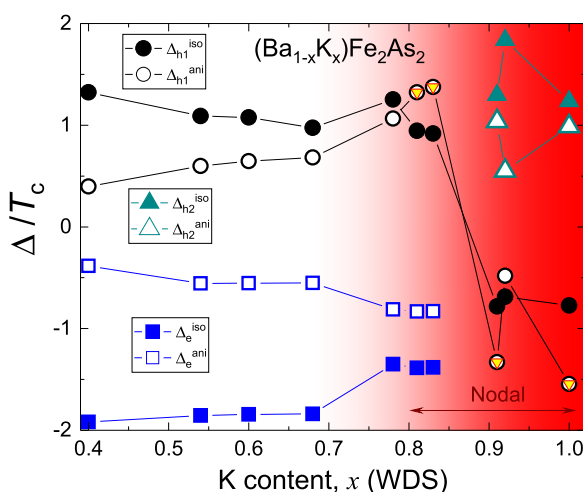


**Figure 14.** Evolution of the superconducting gaps obtained from self-consistent  $t$ -matrix fitting. The assumed electronic structure is described in figure 13. As long as the isotropic part is greater than the anisotropic part, the state is nodeless (that is, for  $x < 0.8$ ). In the opposite limit, the nodes appear. This is shown by the inscribed triangles for the  $h1$  contribution. Consequently, the  $s_{\pm}$  pairing switches from hole-electron pockets below the Lifshitz transition to hole-hole above. For details, refer to [40]. Adapted from [40]. © The Authors, some rights reserved; exclusive licensee American Association for the Advancement of Science. Distributed under a Creative Commons Attribution Non-Commercial License 4.0 (CC BY-NC).

(NMR) studies are consistent with the nodal small gaps and nodeless large gaps [139]. According to the analysis of the low-temperature behavior of the London penetration depth, the superconducting gap of  $\text{SrFe}_2(\text{As}_{1-x}\text{P}_x)_2$  is consistent with the

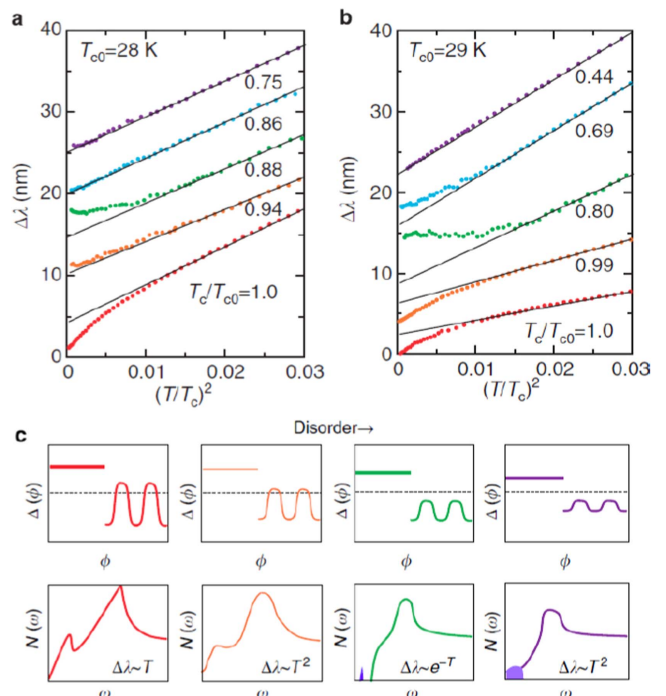


**Figure 15.** Effect of electron irradiation on the low-temperature penetration depth  $\Delta\lambda$  of two samples of  $\text{BaFe}_2(\text{As}_{1-x}\text{P}_x)_2$ : (a)  $T_{c0} = 28$  K and (b)  $T_{c0} = 29$  K. Each curve is shifted vertically for clarity. Lines are the  $T^2$  dependence fits at high temperatures. (c) Schematic of  $s_{\pm}$  order parameter versus azimuthal angle  $\phi$  (top row), and density of states  $N$  versus energy  $\omega$  (bottom row) with increasing irradiation dosage (from left to right). Reprinted with permission from Macmillan Publishers Ltd: Nature Communications [39], Copyright 2014.

presence of line nodes in the gap [140], which is very similar to what is observed with  $\text{BaFe}_2(\text{As}_{1-x}\text{P}_x)_2$ .

In order to understand the origin of the nodal gap, Strehlow *et al* [69] studied the effect of electron irradiation by measuring the London penetration depth before and after irradiation. As shown in figure 24, the electron irradiation effectively suppressed the  $T_c$  of optimally doped  $\text{SrFe}_2(\text{As}_{1-x}\text{P}_x)_2$  ( $x = 0.35$ ). Upon irradiation, the low-temperature penetration depth shows an increase in the power law exponent ( $n$ ). Interestingly, this exponent exceeds the value of  $n = 2$  (figure 25), thus suggesting that the nodes in the superconducting gap are of the accidental type, not symmetry-imposed. In figure 26, the  $\Delta T_c$  and  $\Delta T_c/T_{c0}$  are plotted against irradiation dose for only sample A (higher  $T_c$ , clean sample). This will be compared with other 122 compounds later in the discussion section of this paper. Due to the lack of resistivity data,  $g^\lambda$  is not calculated.

### 3.6. Electron-doped $\text{Ba}(\text{Fe}_{1-x}\text{Co}_x)_2\text{As}_2$

The competition between superconductivity and the magnetic phase has been intensively investigated in electron-doped  $\text{Ba}(\text{Fe}_{1-x}\text{Co}_x)_2\text{As}_2$  [6–8]. A clear separation between the temperatures of structural transition ( $T_s$ ) and the magnetic phase transition ( $T_N$ ) with doping is found, as shown in figure 3(e) [99], which is different from the compounds with hole-doping and isovalent substitution.

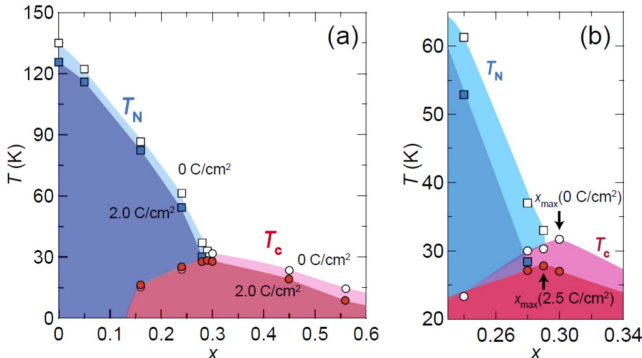


**Figure 16.** (a) Doping phase diagram of  $\text{BaFe}_2(\text{As}_{1-x}\text{P}_x)_2$  for 0 and  $2.0 \text{ C cm}^{-2}$  of electron irradiations. (b) Zoom of the region of nearly optimally doped composition for 0 and  $2.5 \text{ C cm}^{-2}$ . The arrow (maximum  $T_c$ ) moves toward lower composition, indicating the shift of the superconducting dome upon irradiation. Reprinted with permission from [133].

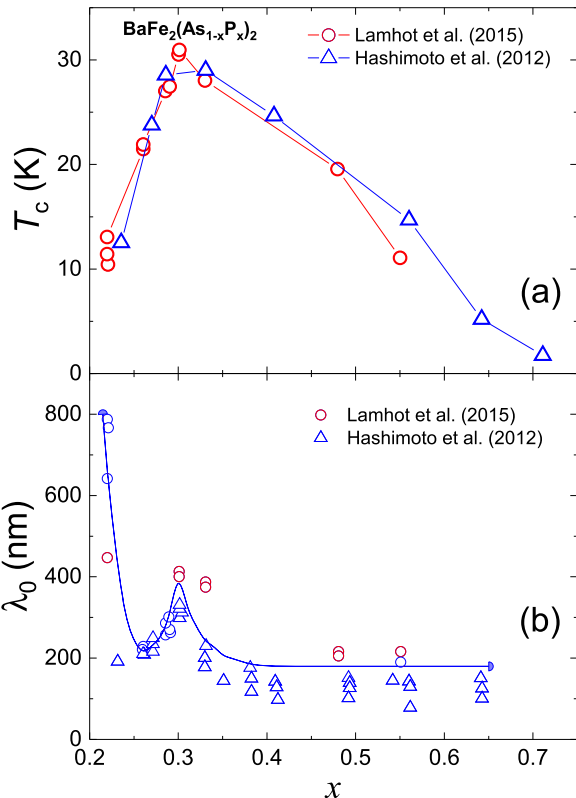


**Figure 17.** (a)  $T_c$  and (b) zero-temperature penetration depth  $\lambda_0$  versus  $x$  in  $\text{BaFe}_2(\text{As}_{1-x}\text{P}_x)_2$ . Data from [96, 134].

The effect of electron irradiation on  $\text{Ba}(\text{Fe}_{1-x}\text{Co}_x)_2\text{As}_2$  was mainly investigated by van der Beek *et al* [141]. The electron irradiation effectively suppresses the  $T_c$  of  $\text{Ba}(\text{Fe}_{1-x}\text{Co}_x)_2\text{As}_2$ , as shown in figure 27. The largest suppression occurs in heavily underdoped and overdoped regions in which the gap is strongly anisotropic and nodal [142, 143]. Similar to other 122 compounds, the suppression is the weakest near the optimal doping region. Since there are no reports on variation of resistivity upon electron irradiation for various compositions, van der Beek *et al* [141] estimated the scattering parameter ( $z\Gamma/2\pi T_c$ ) based on the

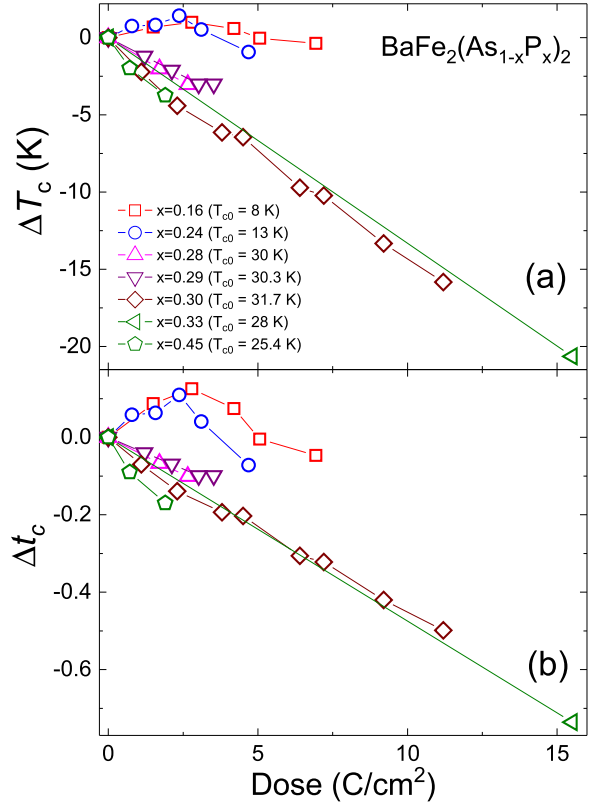


**Figure 18.** Suppression of  $T_c$ : (a)  $\Delta T_c$  and (b)  $\Delta t_c = \Delta T_c / T_{c0}$  of  $\text{BaFe}_2(\text{As}_{1-x}\text{P}_x)_2$  upon electron irradiation. Data from [133]. Data of  $x = 0.25$  and  $0.33$ , and extended data of  $x = 0.30$  (dose  $> 6.4 \text{ C cm}^{-2}$ ), are directly obtained from the authors of [133], and are presented with permission.

density of states, effective mass, atomic point defect density, scattering angle, and so on. While they mentioned that  $\delta R/R \sim 0.05[\text{C cm}^{-2}]^{-1}$ , the actual variations of resistivity ( $\Delta\rho$ ) are not available for all compositions. Nakajima *et al* [61] estimated the dimensionless parameter based on  $\Delta\rho$  by proton irradiation, which is likely to result in clusters of defects instead of point defects. Since we limit our scope to electron irradiation, the  $g^\lambda$  of  $\text{Ba}(\text{Fe}_{1-x}\text{Co}_x)_2\text{As}_2$  is not estimated.

Van der Beek *et al* [141] also used the microwave cavity perturbation technique to measure surface impedance, and studied the variation of the superfluid density of the optimally doped  $\text{Ba}(\text{Fe}_{1-x}\text{Co}_x)_2\text{As}_2$  ( $x = 0.075$ ) upon electron irradiation (see figure 28). The normalized frequency shift, which is proportional to the superfluid density  $n_s \propto \lambda^{-2}$ , shows little to no change upon irradiation, while  $T_c$  drops by 10%. This suggests that the isotropic superconducting gaps with  $s_\pm$  pairing symmetry are intact upon irradiation.

### 3.7. Electron-doped $\text{Ba}(\text{Fe}_{1-x}\text{Ni}_x)_2\text{As}_2$

$\text{Ba}(\text{Fe}_{1-x}\text{Ni}_x)_2\text{As}_2$  is an electron-doped 122 FeSC [144] in which every Ni donates two electrons, which is in contrast to Co substitution where only one electron is donated [145]. Similar to other FeSCs, the  $\text{Ba}(\text{Fe}_{1-x}\text{Ni}_x)_2\text{As}_2$  system shows a superconducting dome with the total suppression of static antiferromagnetic order near the optimal doping level  $x \sim 0.5$

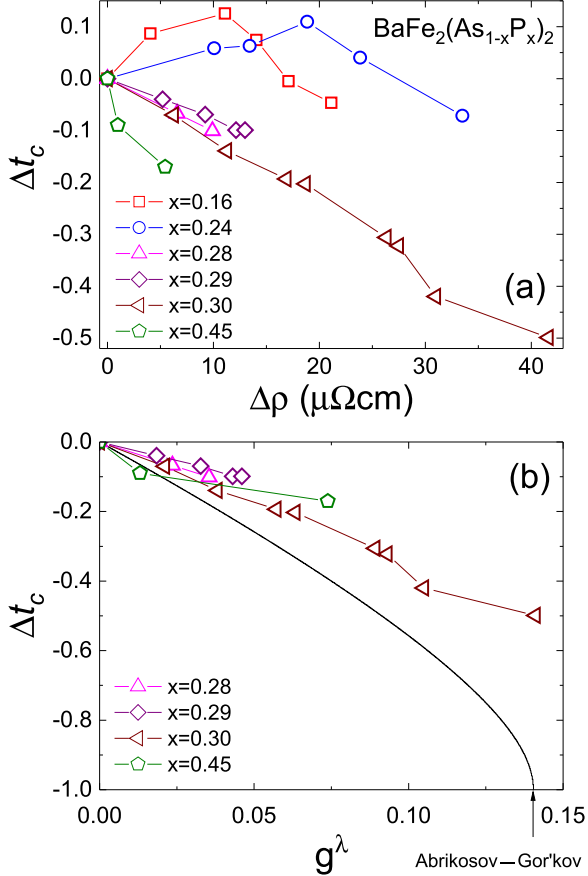


**Figure 19.**  $\Delta t_c = \Delta T_c/T_{c0}$  of  $\text{BaFe}_2(\text{As}_{1-x}\text{P}_x)_2$  versus (a)  $\Delta\rho$  [133] and (b) the dimensionless scattering parameter ( $g^\lambda$ ) calculated following equation (9). The solid line is from the Abrikosov–Gor'kov calculation.

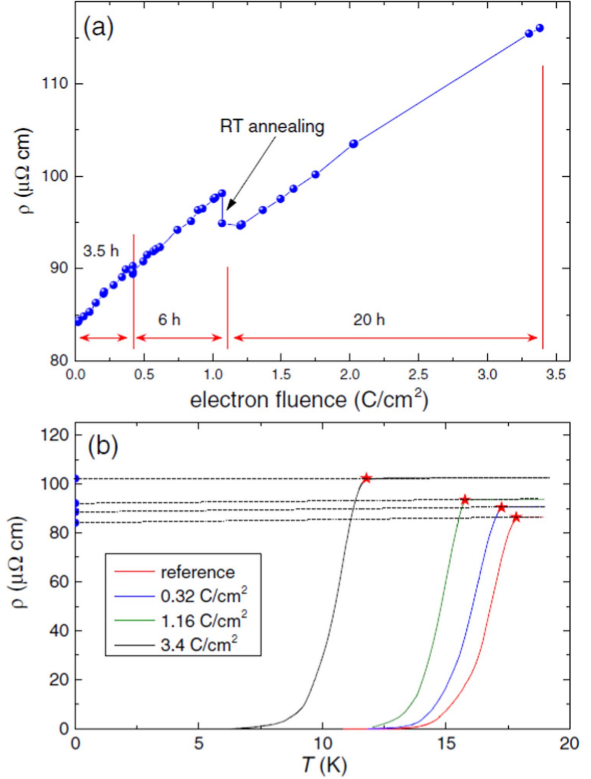


**Figure 21.** (a) *In situ* measurements of resistivity in  $\text{Ba}(\text{Fe}_{1-x}\text{Ru}_x)_2\text{As}_2$  ( $x = 0.24$ ) at  $T \approx 22 \text{ K}$  as a function of the irradiation dose. The breaks in the curve correspond to the extraction of the sample, and warming it up to room temperature (RT) results in a partial annealing of the defects. (b) *Ex situ* measurements of resistivity versus temperature between the irradiation runs. Dashed lines show linear extrapolation of  $\rho(T)$  from above  $T_c$  to  $T = 0 \text{ K}$ . Reprinted figure with permission from [68], Copyright 2014 by the American Physical Society. CC-BY 3.0.

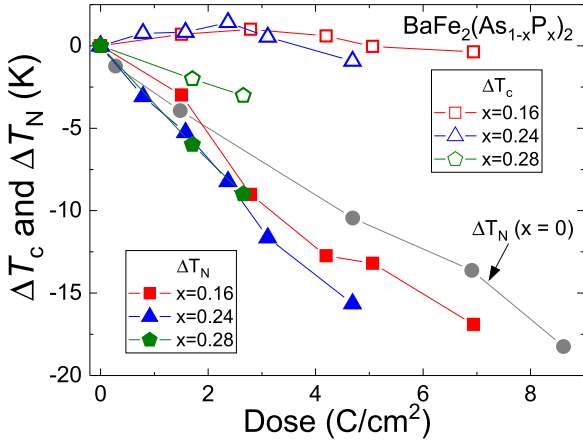


**Figure 20.** Comparison between  $\Delta T_c$  and  $\Delta T_N$  upon electron irradiation. Data from [133]. Data of  $x = 0.25$  are directly obtained from the authors of [133], and are presented with permission.

[100]. As commonly found in electron-doped systems, the separation between structural ( $T_s$ ) and magnetic ( $T_m$ ) transitions is also observed in this compound. However, the details vary across studies. A high-resolution synchrotron x-ray and neutron scattering study showed a sharp first-order like

disappearance of magnetic ordering above the optimally doped region, and the authors interpreted it as an avoidance of quantum criticality [146] (see figure 3(f)). In an NMR study, the separation was interpreted as evidence of two critical points at  $x_{c1} = 0.05$  and  $x_{c2} = 0.07$ , respectively. Since the highest  $T_c$  is found around  $x_{c1}$ , it is claimed that the superconductivity is more closely tied to the magnetic quantum critical point.

The effect of electron irradiation on  $\text{Ba}(\text{Fe}_{1-x}\text{Ni}_x)_2\text{As}_2$  ( $x = 0.045$ ) was studied by van der Beek *et al* [141]. The suppression of  $T_c$  is shown in figure 29. Since the resistivity data are not available, the dimensionless parameter ( $g^\lambda$ ) is not estimated.

#### 4. Discussion

In this section, we summarize and compare the  $T_c$  suppression rates of various 122 FeSCs upon electron irradiation. We use the normalized transition temperature  $t_c = T_c/T_{c0}$ , where  $T_{c0}$  is the value in pristine samples. In figure 30 we compare  $\Delta t_c/\Delta\text{dose}$  versus  $x$  of all six compounds. For convenience of comparison, the range of  $x$  is limited to superconducting compositions only. The

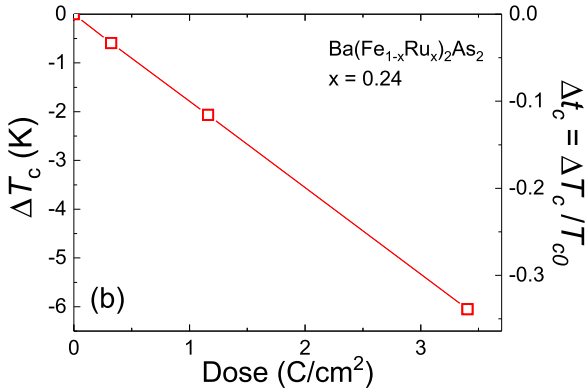


**Figure 22.** Suppression of  $T_c$ :  $\Delta T_c$  (left) and  $\Delta t_c = \Delta T_c / T_{c0}$  (right) of  $\text{Ba}(\text{Fe}_{1-x}\text{Ru}_x)_2\text{As}_2$  ( $x = 0.24$ ) upon electron irradiation. Data from [68].

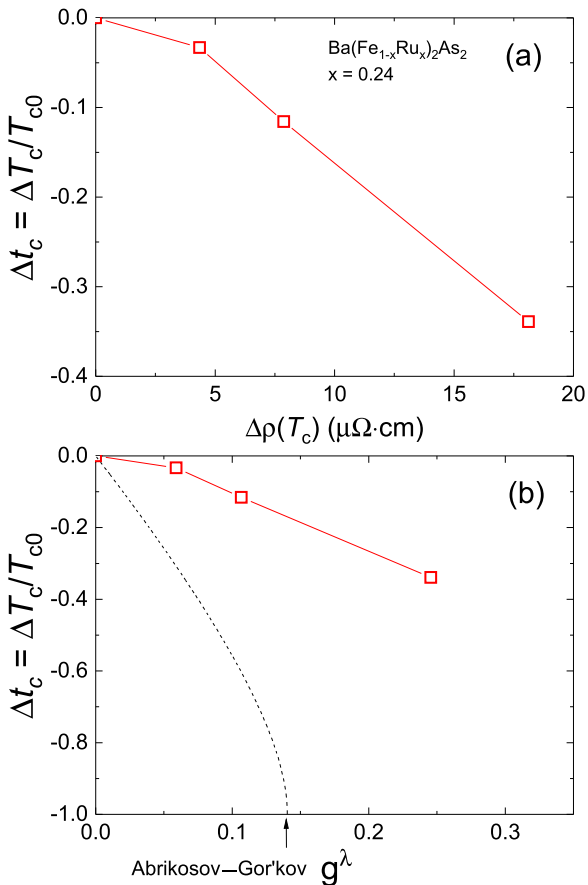


**Figure 23.** (a)  $\Delta t_c = \Delta T_c / T_{c0}$  versus  $\Delta \rho$  of  $\text{Ba}(\text{Fe}_{1-x}\text{Ru}_x)_2\text{As}_2$  ( $x = 0.24$ ) upon electron irradiation. The dimensionless scattering rate  $g^\lambda$  is calculated from the resistivity and penetration depth following equation (9). Here,  $\lambda_0 = 200 \text{ nm}$  was used. The Abrikosov–Gor'kov calculation is also shown for comparison. Data from [68].

schematic  $T_c - x$  phase diagram is shown in panel (a), with the optimally doped region (blue shaded area) and two ends of the superconducting dome (gray shaded area) marked. For panels (b)–(g), both ends in the gray area are the end compositions of the superconducting dome, and the blue area indicates the optimally doped composition. Systematic studies that cover more than 50% of superconducting

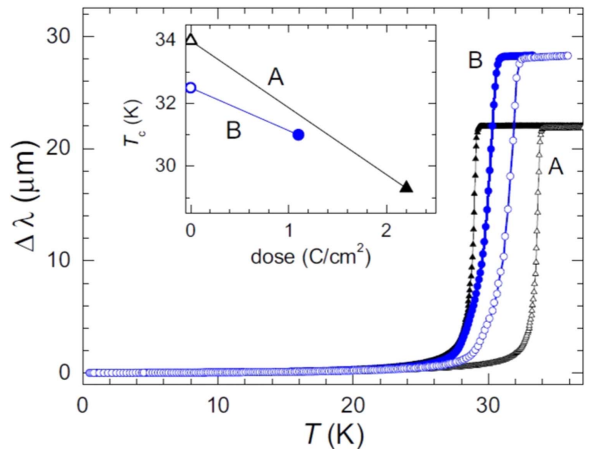


**Figure 24.** Full temperature range variation of  $\Delta\lambda(T)$ , in two single crystals of  $\text{SrFe}_2(\text{As}_{1-x}\text{P}_x)_2$ ,  $x = 0.35$ ; A (black triangles) and B (blue circles) represent before (open symbols) and after (solid symbols) electron irradiation with doses of 2.2 and  $1.1 \text{ C cm}^{-2}$ , respectively. The inset shows the change in  $T_c$  as a function of the irradiation dose. Reprinted figure with permission from [69], Copyright 2014 by the American Physical Society.

compositions are only available for  $(\text{Ba}_{1-x}\text{K}_x)\text{Fe}_2\text{As}_2$  and  $\text{Ba}(\text{Fe}_{1-x}\text{Co}_x)_2\text{As}_2$ . For the case of  $(\text{Ba}_{1-x}\text{K}_x)\text{Fe}_2\text{As}_2$ , the value of the  $\Delta t_c/\Delta\text{dose}$  is small near optimal doping, and becomes larger as it goes toward underdoped and overdoped compositions. In particular, the pure  $\text{KFe}_2\text{As}_2$  shows the largest value:  $\Delta t_c/\Delta\text{dose} \approx 0.5$ . However, the  $\Delta t_c/\Delta\text{dose}$  of  $\text{Ba}(\text{Fe}_{1-x}\text{Co}_x)_2\text{As}_2$  in panel (f) is small ( $< 0.05$ ), and does not change much with compositions. These small values can be attributed to the fact that the pristine  $\text{Ba}(\text{Fe}_{1-x}\text{Co}_x)_2\text{As}_2$  is already in the dirty limit, as shown in figure 4, and therefore additional disorder introduced by electron irradiation is less effective in changing its properties. For  $\text{BaFe}_2(\text{As}_{1-x}\text{P}_x)_2$ , only nearly optimal and slightly overdoped compositions were studied. While the doping dependence of  $\Delta t_c/\Delta\text{dose}$  is similar to  $(\text{Ba}_{1-x}\text{K}_x)\text{Fe}_2\text{As}_2$ , the comparison is not conclusive due to the limited range of compositions studied. Studies for singular compositions were only performed for  $\text{Ba}(\text{Fe}_{1-x}\text{Ru}_x)_2\text{As}_2$  and  $\text{Ba}(\text{Fe}_{1-x}\text{Ni}_x)_2\text{As}_2$ , and therefore further studies are needed to find their doping dependences.

Another interesting aspect in figure 30 is that in general the optimally doped compositions of all 122 FeSCs commonly show lowest suppression with similar low values ( $< 0.05$ ). To get additional insight into this fact, the data for only optimally doped compositions are replotted in figure 31(a)  $\Delta T_c$  and (b)  $\Delta t_c = \Delta T_c / T_{c0}$  versus increasing dosage. Two different trends of  $T_c$  suppression are observed (panel (a)). The first group includes hole-doped and isovalent-substituted compounds:  $(\text{Ba}_{1-x}\text{K}_x)\text{Fe}_2\text{As}_2$ ,  $\text{BaFe}_2(\text{As}_{1-x}\text{P}_x)_2$ ,  $\text{SrFe}_2(\text{As}_{1-x}\text{P}_x)_2$ , and  $\text{Ba}(\text{Fe}_{1-x}\text{Ru}_x)_2\text{As}_2$ . The second group includes electron-doped compounds:  $\text{Ba}(\text{Fe}_{1-x}\text{Co}_x)_2\text{As}_2$  and  $\text{Ba}(\text{Fe}_{1-x}\text{Ni}_x)_2\text{As}_2$ . The former group commonly shows a suppression rate of  $\Delta T_c = -4 \text{ K} [\text{C cm}^{-2}]^{-1}$ , regardless of different  $T_c$  and different chemical contents. The reason why these different compounds show similar suppression behavior in the absolute Kelvin scale remains unclear. For the latter

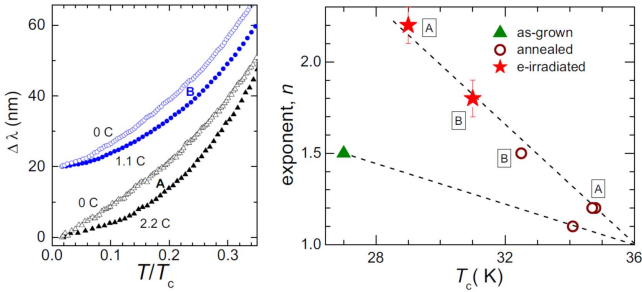


**Figure 25.** (a) Low-temperature variation of  $\Delta\lambda$  in  $\text{SrFe}_2(\text{As}_{1-x}\text{P}_x)_2$  ( $x = 0.35$ ) versus reduced temperature  $T/T_c$ . The data before and after irradiation are shown by open and solid symbols, respectively. An offset of 20 nm is applied to avoid overlapping. (b) Exponent  $n$  of the power law fit of  $\Delta\lambda$ . Note the significantly smaller exponents for as-grown and annealed samples compared to the samples with irradiation defects. Reprinted figure with permission from [69]. Copyright 2014 by the American Physical Society.

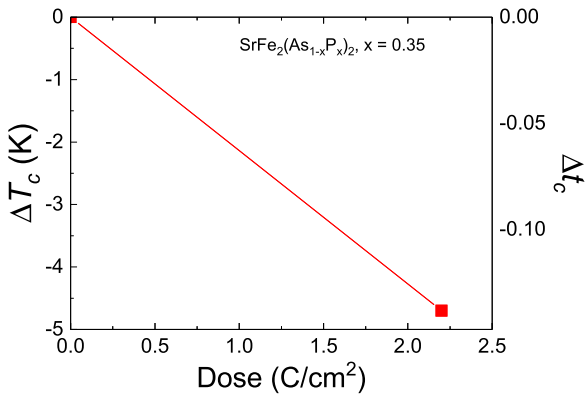


**Figure 26.** Suppression of  $T_c$ :  $\Delta T_c$  (left) and  $\Delta t_c = \Delta T_c / T_{c0}$  (right) of  $\text{SrFe}_2(\text{As}_{1-x}\text{P}_x)_2$  ( $x = 0.35$ ) upon electron irradiation. The sample A with a higher  $T_c$  is plotted. Data from [69].

group of electron-doped compounds, the rate is about three times smaller. This slow suppression of  $T_c$  in electron-doped compounds can be understood by the fact that the pristine samples are already in the dirty limit, as clearly seen in the resistivity measurement in the bottom panels of figure 4.

In addition to  $\Delta T_c$ , figure 32 shows a comparison of  $\Delta T_N$  for underdoped  $(\text{Ba}_{1-x}\text{K}_x)\text{Fe}_2\text{As}_2$  and  $\text{BaFe}_2(\text{As}_{1-x}\text{P}_x)_2$ . Interestingly, these different compounds show similar suppression rates upon electron irradiation even though their  $T_{N0}$  and chemical contents are notably different. This can be an indication that the scattering mechanism in the SDW phase are similar, and produce a similar response upon electron irradiation.

In figure 33, the suppression rates per resistivity increase ( $t_c/\Delta\rho$ ) in  $(\text{Ba}_{1-x}\text{K}_x)\text{Fe}_2\text{As}_2$ ,  $\text{BaFe}_2(\text{As}_{1-x}\text{P}_x)_2$ , and  $\text{Ba}(\text{Fe}_{1-x}\text{Ru}_x)_2\text{As}_2$  are summarized. Panel (a) of  $(\text{Ba}_{1-x}\text{K}_x)\text{Fe}_2\text{As}_2$  shows a rather complete doping dependence. The largest value of  $t_c/\Delta\rho$  is obtained in the pure  $\text{KFe}_2\text{As}_2$ , and the smallest value is obtained in the nearly optimally doped compounds. In general, the value of  $t_c/\Delta\rho$  increases away from the optimally doped composition. A similar trend is observed in  $\text{BaFe}_2(\text{As}_{1-x}\text{P}_x)_2$ , but further experimental data in overdoped and underdoped compositions are needed. In

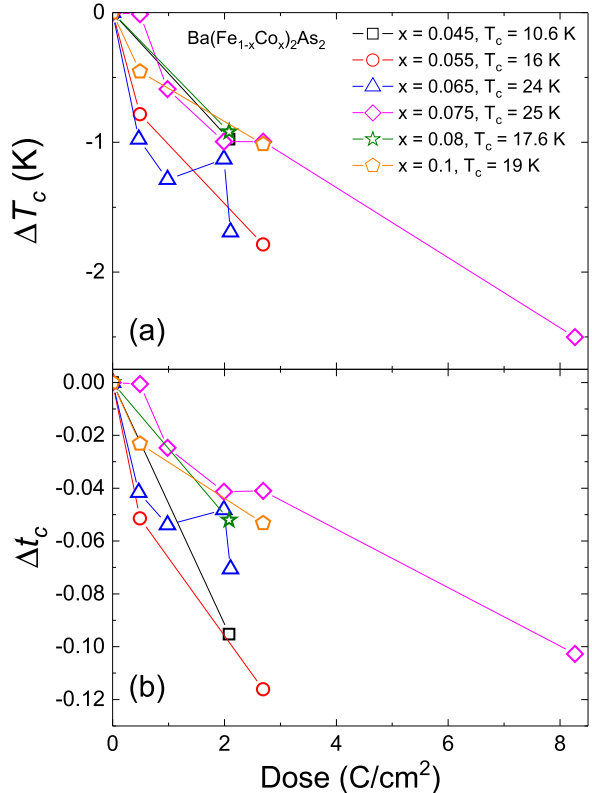


**Figure 27.** Suppression of  $T_c$ : (a)  $\Delta T_c$  and (b)  $\Delta t_c = \Delta T_c / T_{c0}$  versus irradiation dose in  $\text{Ba}(\text{Fe}_{1-x}\text{Co}_x)_2\text{As}_2$ . Data from [141].

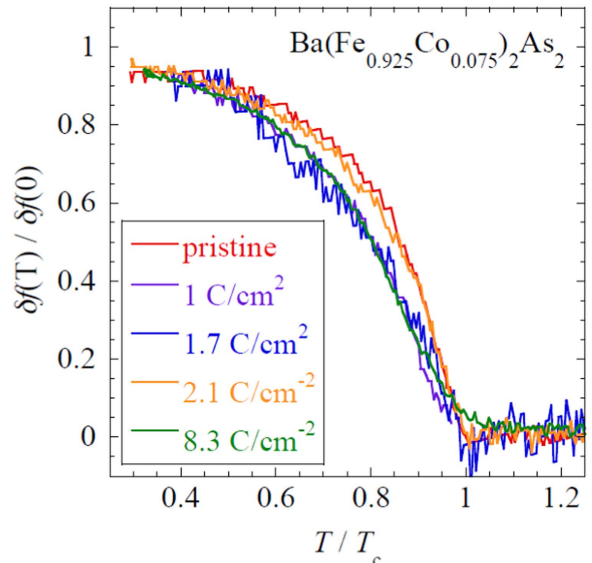


**Figure 28.** Superfluid density of  $\text{Ba}(\text{Fe}_{1-x}\text{Co}_x)_2\text{As}_2$  ( $x = 0.075$ ) upon electron irradiation by using the microwave cavity perturbation technique. Reproduced from [141]. © IOP Publishing Ltd. All rights reserved.

$\text{Ba}(\text{Fe}_{1-x}\text{Ru}_x)_2\text{As}_2$ , only one data point in the underdoped region is available. It is comparable to the data for underdoped  $(\text{Ba}_{1-x}\text{K}_x)\text{Fe}_2\text{As}_2$  and  $\text{BaFe}_2(\text{As}_{1-x}\text{P}_x)_2$ .

In figure 34, the  $\Delta t_c/\Delta g$  of the three compounds in figure 33 is summarized. In  $(\text{Ba}_{1-x}\text{K}_x)\text{Fe}_2\text{As}_2$  (panel (b)), the most underdoped compound shows the largest value, and then

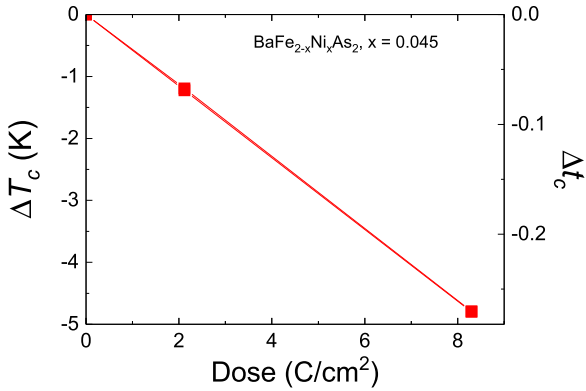


**Figure 29.** Suppression of  $T_c$ :  $\Delta T_c$  (left) and  $\Delta t_c = \Delta T_c/T_{c0}$  (right) versus dose of  $\text{BaFe}_{2-x}\text{Ni}_x\text{As}_2$ . Data from [141].

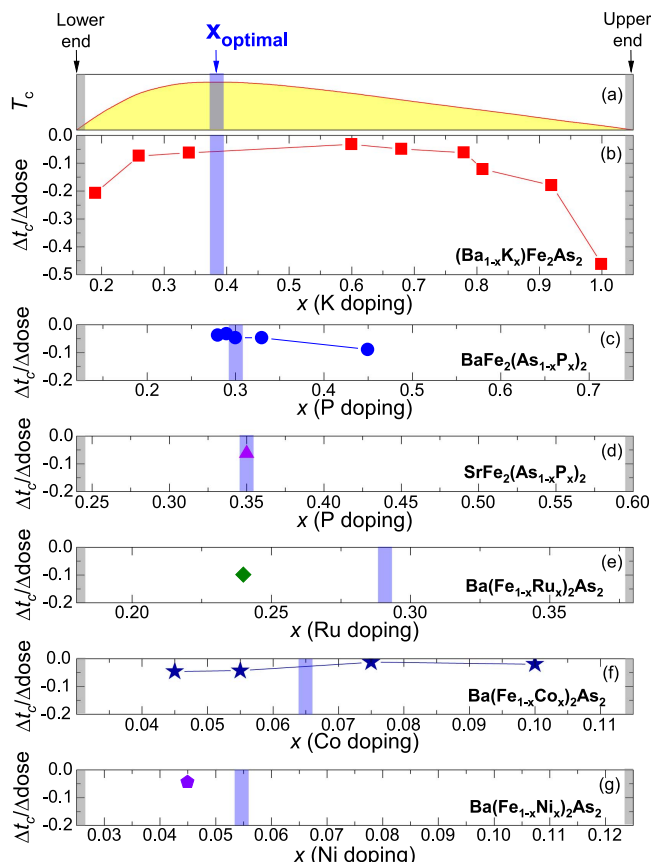


**Figure 30.**  $\Delta t_c/\Delta \text{dose}$  versus  $x$  of 122 FeSCs. (a) Schematic  $T_c$  versus  $x$  phase diagram. (b)–(g)  $\Delta t_c/\Delta \text{dose}$  versus  $x$  of  $(\text{Ba}_{1-x}\text{K}_x)\text{Fe}_2\text{As}_2$ ,  $\text{BaFe}_2(\text{As}_{1-x}\text{P}_x)_2$ ,  $\text{SrFe}_2(\text{As}_{1-x}\text{P}_x)_2$ ,  $\text{Ba}(\text{Fe}_{1-x}\text{Ru}_x)_2\text{As}_2$ ,  $\text{Ba}(\text{Fe}_{1-x}\text{Co}_x)_2\text{As}_2$ , and  $\text{Ba}(\text{Fe}_{1-x}\text{Ni}_x)_2\text{As}_2$ , respectively. Note that the blue shaded areas indicate the optimally doped compositions ( $x_{\text{optimal}}$ ) with maximum  $T_c$ . Approximate upper and lower ends of the superconducting dome ( $T_c = 0$ ) are marked by the gray shaded areas.

weakens toward the nearly optimal and slightly overdoped regions. Since  $\lambda_0$  values are not available for the overdoped region, dimensionless parameter  $g^\lambda$  in the overdoped region is not estimated. In general, one can find that  $\Delta t_c/\Delta g$  of  $(\text{Ba}_{1-x}\text{K}_x)\text{Fe}_2\text{As}_2$  has larger values for most compositions

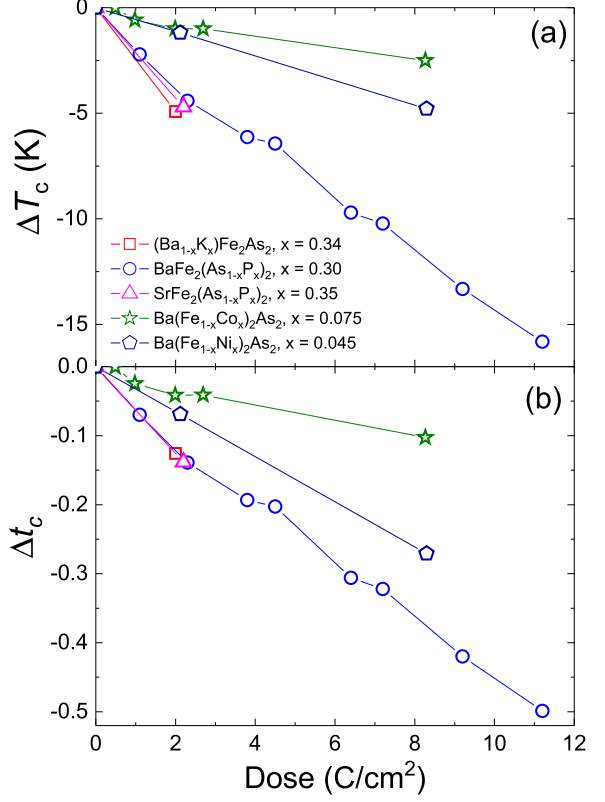


**Figure 31.** Suppression of  $T_c$ : (a)  $\Delta T_c$  and (b)  $\Delta t_c = \Delta T_c/T_{c0}$  upon electron irradiation in optimally doped 122 FeSCs.

than those of  $\text{BaFe}_2(\text{As}_{1-x}\text{P}_x)_2$ . For further comparison, the  $\Delta t_c$  versus  $g^\lambda$  of the nearly optimally doped region is plotted in figure 35(b). It is clear that the suppression of  $T_c$  is larger in  $\text{BaFe}_2(\text{As}_{1-x}\text{P}_x)_2$ . However, in all cases, the suppression rate is slower than the Abrikosov–Gor’kov value.

In figure 36, the key parameters of optimally doped 122 FeSCs are summarized. Panel (a) shows the  $T_c$  of all compounds ranging from the highest value in  $(\text{Ba}_{1-x}\text{K}_x)\text{Fe}_2\text{As}_2$  to the lowest in  $\text{Ba}(\text{Fe}_{1-x}\text{Ni}_x)_2\text{As}_2$ . Since the initial resistivity values (as an initial disorder before irradiation) are important to understand the post-irradiated properties,  $\rho_0$  at 40 K for pristine samples are compared in panel (b).  $(\text{Ba}_{1-x}\text{K}_x)\text{Fe}_2\text{As}_2$ ,  $\text{BaFe}_2(\text{As}_{1-x}\text{P}_x)_2$ , and  $\text{SrFe}_2(\text{As}_{1-x}\text{P}_x)_2$  have rather low resistivity values ( $< 50 \mu\Omega\text{ cm}$ ) while electron-doped  $\text{Ba}(\text{Fe}_{1-x}\text{Co}_x)_2\text{As}_2$  and  $\text{Ba}(\text{Fe}_{1-x}\text{Ni}_x)_2\text{As}_2$  have quite large values ( $> 100 \mu\Omega\text{ cm}$ ), which indicates that they are already in the dirty limit at the pristine state. In panel (c), the values of  $\Delta T_c/\text{dose}$  are compared. In general, the electron-doped compounds,  $\text{Ba}(\text{Fe}_{1-x}\text{Co}_x)_2\text{As}_2$  and  $\text{Ba}(\text{Fe}_{1-x}\text{Ni}_x)_2\text{As}_2$ , undergo the least change upon electron irradiation mainly due to the pre-existing disorder (dirty limit), while hole-doped and isovalent-substituted compounds show larger changes. In panel (d), the  $\Delta t_c/\text{dose}$  of  $(\text{Ba}_{1-x}\text{K}_x)\text{Fe}_2\text{As}_2$ ,  $\text{BaFe}_2(\text{As}_{1-x}\text{P}_x)_2$ , and  $\text{SrFe}_2(\text{As}_{1-x}\text{P}_x)_2$  show similar values, while  $\text{Ba}(\text{Fe}_{1-x}\text{Co}_x)_2\text{As}_2$  has the smallest value. In panel (e),  $\Delta T_c/\text{dose}$  is only shown for  $(\text{Ba}_{1-x}\text{K}_x)\text{Fe}_2\text{As}_2$  and  $\text{BaFe}_2(\text{As}_{1-x}\text{P}_x)_2$ . It is clear that the suppression is stronger in  $\text{BaFe}_2(\text{As}_{1-x}\text{P}_x)_2$ .

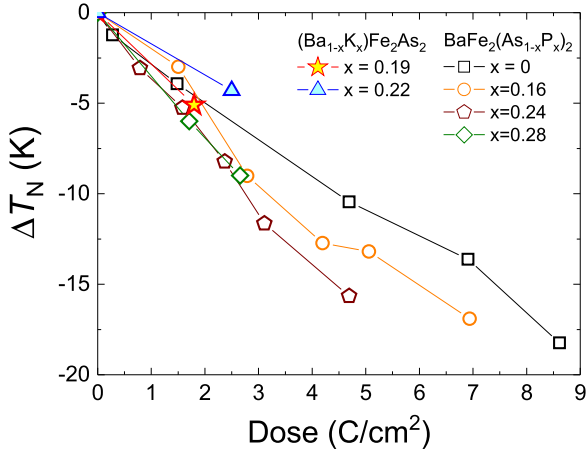


**Figure 32.** Comparison of  $\Delta T_N$  upon electron irradiation in underdoped  $(\text{Ba}_{1-x}\text{K}_x)\text{Fe}_2\text{As}_2$  and  $\text{BaFe}_2(\text{As}_{1-x}\text{P}_x)_2$ .

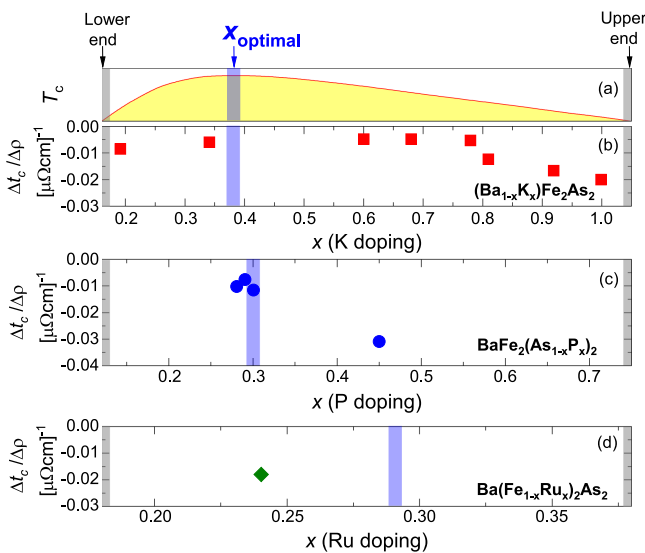


**Figure 33.**  $\Delta t_c/\Delta \rho$  versus compositions of 122 FeSCs. (a) Schematic  $T_c$  versus  $x$  phase diagram. (b)–(d)  $\Delta t_c/\Delta \rho$  versus  $x$  in  $(\text{Ba}_{1-x}\text{K}_x)\text{Fe}_2\text{As}_2$ ,  $\text{BaFe}_2(\text{As}_{1-x}\text{P}_x)_2$ , and  $\text{Ba}(\text{Fe}_{1-x}\text{Ru}_x)_2\text{As}_2$ , respectively. Note that the blue shaded areas indicate the optimally doped compositions ( $x_{\text{optimal}}$ ) with maximum  $T_c$ . Approximate upper and lower ends of the superconducting dome ( $T_c = 0$ ) are marked by the gray shaded areas.

## 5. Conclusions

In this article, we reviewed the use of electron irradiation that induces controlled point-like disorders as a phase-sensitive probe to study superconductivity in the 122 family of FeSCs. The simultaneous measurements of changes in the superconducting transition temperature and in the low temperature variation of the London penetration depth lead to the experimental conclusion that  $s_{\pm}$  pairing is robust and ubiquitous in FeSCs. Substantial sensitivity to nonmagnetic disorder also means that all experimental studies of the superconducting gap structure should be analyzed by taking the effect of impurity scattering into account. While the material may be ‘clean’ in terms of comparison of a normal mean free

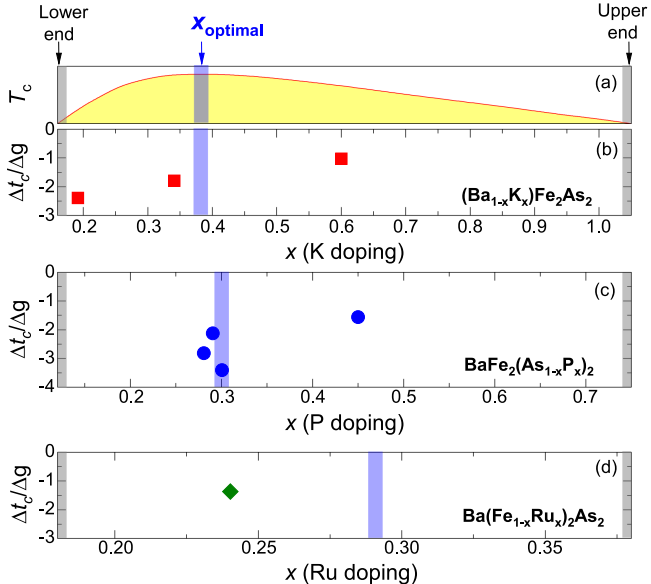


**Figure 34.**  $\Delta t_c/\Delta g$  versus  $x$  of 122 FeSCs. (a) Schematic  $T_c$  versus  $x$  phase diagram. (b)–(d)  $\Delta t_c/\Delta g$  versus  $x$  in  $(\text{Ba}_{1-x}\text{K}_x)\text{Fe}_2\text{As}_2$ ,  $\text{BaFe}_2(\text{As}_{1-x}\text{P}_x)_2$ , and  $\text{Ba}(\text{Fe}_{1-x}\text{Ru}_x)_2\text{As}_2$ , respectively. Note that the blue shaded areas indicate the optimally doped compositions ( $x_{\text{optimal}}$ ) with maximum  $T_c$ . Approximate upper and lower ends of the superconducting dome ( $T_c = 0$ ) are marked by the gray shaded areas.

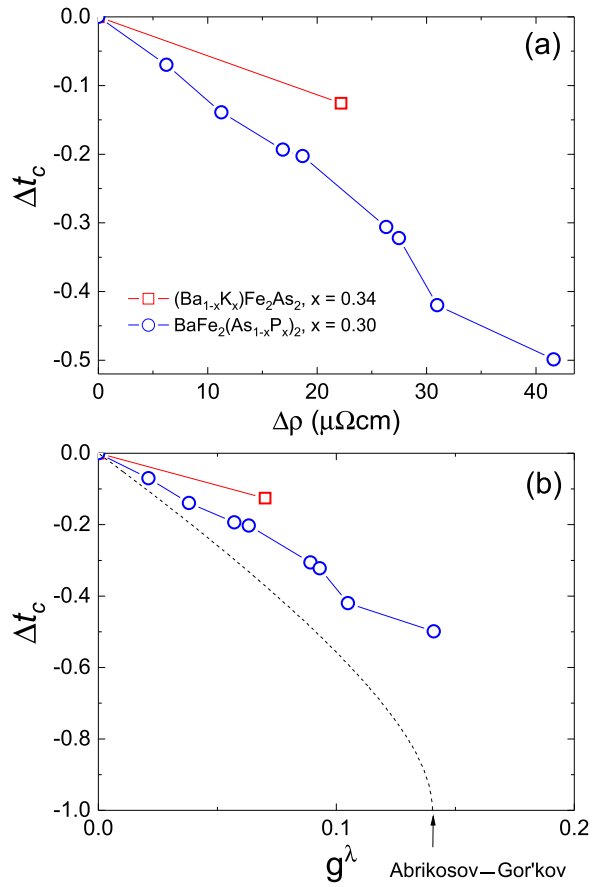


**Figure 35.** Comparison of optimally doped  $\text{Ba}_{1-x}\text{K}_x\text{Fe}_2\text{As}_2$  and  $\text{BaFe}_2(\text{As}_{1-x}\text{P}_x)_2$  compounds: (a)  $\Delta t_c$  versus  $\Delta \rho$  and (b)  $\Delta t_c$  versus the dimensionless scattering parameter ( $g^\lambda$ ) calculated following equation (9).

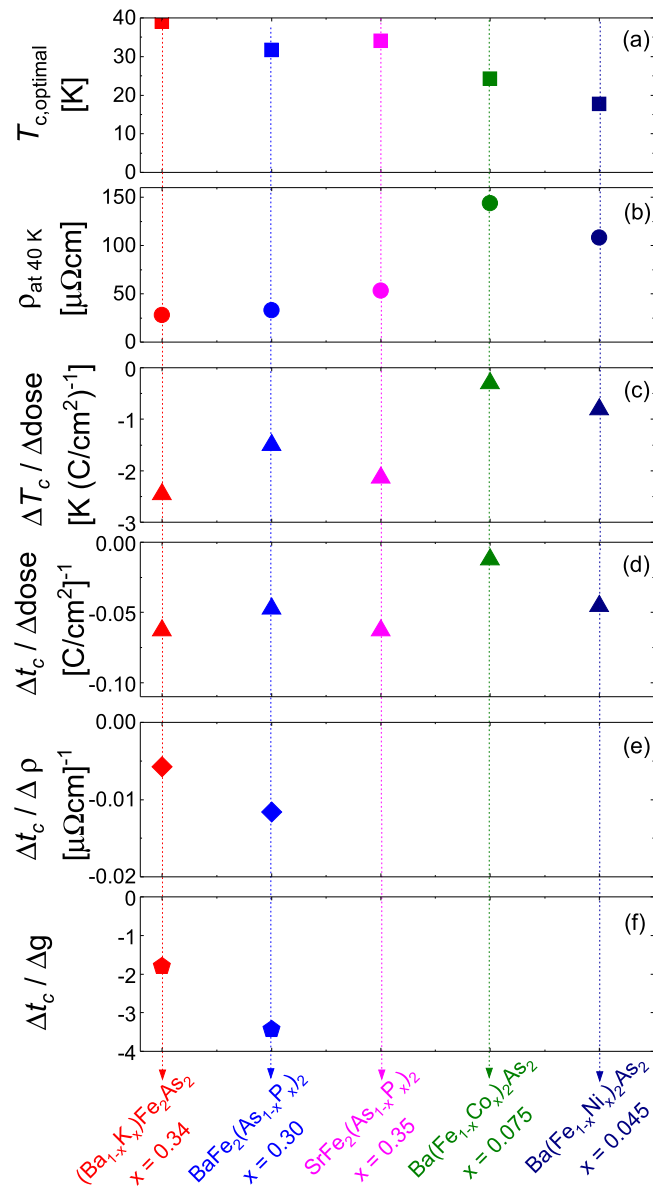


**Figure 36.** Summary of key parameters in optimally doped 122 FeSCs: (a)  $T_c$ , (b)  $\rho$  at 40 K, (c)  $\Delta T_c / \Delta \text{dose}$ , (d)  $\Delta t_c / \Delta \text{dose}$ , (e)  $\Delta t_c / \Delta \rho$ , and (f)  $\Delta t_c / \Delta g$ .

path and very short coherence length, the pair-breaking is significant at any concentration of scattering centers. This will affect the temperature dependence of all thermodynamic, spectroscopic, and transport properties.

## Acknowledgments

We thank P C Canfield, S L Bud'ko, P J Hirschfeld, V G Kogan, T Shibauchi, Y Matsuda, V Mishra, A V Chubukov, S Miyasaka, and C J van der Beek for useful discussion. This work was supported by the US Department of Energy (DOE), Office of Science, Basic Energy Sciences, Materials Science and Engineering Division. Ames Laboratory is operated for the US DOE by Iowa State University under contract #DE-AC02-07CH11358. We thank the SIRIUS team,

O Cavani, B Boizot, V Metayer, and J Losco, for running electron irradiation at École Polytechnique (supported by the EMIR (Réseau national d'accélérateurs pour les Etudes des Matériaux sous Irradiation) network, proposal 11-11-0121, 13-11-0484, 15-5788).

## ORCID iDs

Kyuil Cho <https://orcid.org/0000-0003-2111-6355>  
M A Tanatar <https://orcid.org/0000-0003-2129-9833>  
R Prozorov <https://orcid.org/0000-0002-8088-6096>

## References

- [1] Kamihara Y, Hiramatsu H, Hirano M, Kawamura R, Yanagi H, Kamiya T and Hosono H 2006 *J. Am. Chem. Soc.* **128** 10012
- [2] Kamihara Y, Watanabe T, Hirano M and Hosono H 2008 *J. Am. Chem. Soc.* **130** 3296
- [3] Johnston D C 2010 *Adv. Phys.* **59** 803
- [4] Canfield P C and Bud'ko S L 2010 *Annu. Rev. Condens. Matter Phys.* **1** 27
- [5] Paglione J and Greene R L 2010 *Nat. Phys.* **6** 645
- [6] Hirschfeld P J, Korshunov M M and Mazin I I 2011 *Rep. Prog. Phys.* **74** 124508
- [7] Stewart G R 2011 *Rev. Mod. Phys.* **83** 1589
- [8] Carrington A 2011 *Rep. Prog. Phys.* **74** 124507
- [9] Abrahams E and Si Q 2011 *J. Phys.: Condens. Matter* **23** 223201
- [10] Carrington A 2011 *C. R. Phys.* **12** 502
- [11] Prozorov R and Kogan V G 2011 *Rep. Prog. Phys.* **74** 124505
- [12] Wen H-H and Li S 2011 *Annu. Rev. Condens. Matter Phys.* **2** 121
- [13] Zhang J-l, Jiao L, Chen Y and Yuan H-q 2011 *Front. Phys.* **6** 463
- [14] Chubukov A 2012 *Annu. Rev. Condens. Matter Phys.* **3** 57
- [15] Kordyuk A A 2012 *Low Temp. Phys.* **38** 888
- [16] Song C-L and Hoffman J E 2013 *Curr. Opin. Solid State Mater. Sci.* **17** 39
- [17] Long M and Wei-Qiang Y 2013 *Chin. Phys. B* **22** 087414
- [18] Hao J, Yun-Lei S, Zhu-An X and Guang-Han C 2013 *Chin. Phys. B* **22** 087410
- [19] Carretta P, Renzi R D, Prando G and Sanna S 2013 *Phys. Scr.* **88** 068504
- [20] Zi-Rong Y, Yan Z, Bin-Ping X and Dong-Lai F 2013 *Chin. Phys. B* **22** 087407
- [21] Eremin I, Knolle J, Fernandes R M, Schmalian J and Chubukov A V 2014 *J. Phys. Soc. Japan* **83** 061015
- [22] Charnukha A 2014 *J. Phys.: Condens. Matter* **26** 253203
- [23] Shibauchi T, Carrington A and Matsuda Y 2014 *Annu. Rev. Condens. Matter Phys.* **5** 113
- [24] Dai P 2015 *Rev. Mod. Phys.* **87** 855
- [25] Jasek A, Komeda K, Blachowski A, Ruebenbauer K, Zukrowski J, Bukowski Z and Karpinski J 2015 *Phil. Mag.* **95** 493
- [26] Böhmer A E and Meingast C 2016 *C. R. Phys.* **17** 90
- [27] Palleggi I, Cagliari F and Putti M 2016 *Supercond. Sci. Technol.* **29** 073002
- [28] Gallais Y and Paul I 2016 *C. R. Phys.* **17** 113
- [29] Li J, Guo Y-F, Yang Z-R, Yamaura K, Takayama-Muromachi E, Wang H-B and Wu P-H 2016 *Supercond. Sci. Technol.* **29** 053001

- [30] Martinelli A, Bernardini F and Massidda S 2016 *C. R. Phys.* **17** 5
- [31] Guterding D, Backes S, Tomic M, Jeschke H O and Valenti R 2017 *Phys. Status Solidi B* **254** 1600164
- [32] Fernandes R M and Chubukov A V 2017 *Rep. Prog. Phys.* **80** 014503
- [33] Yi M, Zhang Y, Shen Z-X and Lu D 2017 *Npj Quantum Mater.* **2** 57
- [34] Putti M et al 2010 *Supercond. Sci. Technol.* **23** 034003
- [35] Ma Y 2012 *Supercond. Sci. Technol.* **25** 113001
- [36] Tanabe K and Hosono H 2012 *Japan. J. Appl. Phys.* **51** 010005
- [37] Ma Y 2015 *Physica C* **516** 17
- [38] Hosono H, Yamamoto A, Hiramatsu H and Ma Y 2018 *Mater. Today* **21** 278
- [39] Mizukami Y et al 2014 *Nat. Comm.* **5** 5657
- [40] Cho K et al 2016 *Sci. Adv.* **2** e1600807
- [41] Anderson P W 1959 *J. Phys. Chem. Solids* **11** 26
- [42] Abricosov A A and Gor'kov L P 1961 *Sov. Phys. JETP* **12** 1243
- [43] Balian R and Werthamer N R 1963 *Phys. Rev.* **131** 1553
- [44] Openov L A 1998 *Phys. Rev. B* **58** 9468
- [45] Senga Y and Kontani H 2008 *J. Phys. Soc. Japan* **77** 113710
- [46] Onari S and Kontani H 2009 *Phys. Rev. Lett.* **103** 177001
- [47] Efremov D V, Korshunov M M, Dolgov O V, Golubov A A and Hirschfeld P J 2011 *Phys. Rev. B* **84** 180512
- [48] Fernandes R M, Vavilov M G and Chubukov A V 2012 *Phys. Rev. B* **85** 140512
- [49] Wang Y, Kreisel A, Hirschfeld P J and Mishra V 2013 *Phys. Rev. B* **87** 094504
- [50] Chen X, Mishra V, Maiti S and Hirschfeld P J 2016 *Phys. Rev. B* **94** 054524
- [51] Korshunov M M, Togushova Y N and Dolgov O V 2017 *Phys.-Usp.* **59** 1211
- [52] Tsuei C C and Kirtley J R 2000 *Rev. Mod. Phys.* **72** 969
- [53] Aloul H, Bobroff J, Gabay M and Hirschfeld P J 2009 *Rev. Mod. Phys.* **81** 45
- [54] Damask A C and Dienes G J 1963 *Point Defects in Metals* (London: Gordon & Breach Science)
- [55] Nakajima Y, Tsuchiya Y, Taen T, Tamegai T, Okayasu S and Sasase M 2009 *Phys. Rev. B* **80** 012510
- [56] Civale L, Marwick A D, Worthington T K, Kirk M A, Thompson J R, Krusin-Elbaum L, Sun Y, Clem J R and Holtzberg F 1991 *Phys. Rev. Lett.* **67** 648
- [57] Konczykowski M, Rullier-Albenque F, Yacoby E R, Shaulov A, Yeshurun Y and Lejay P 1991 *Phys. Rev. B* **44** 7167
- [58] Kim H et al 2010 *Phys. Rev. B* **82** 060518
- [59] Prozorov R, Tanatar M A, Roy B, Ni N, Bud'ko S L, Canfield P C, Hua J, Welp U and Kwok W K 2010 *Phys. Rev. B* **81** 094509
- [60] Murphy J, Tanatar M A, Kim H, Kwok W, Welp U, Graf D, Brooks J S, Bud'ko S L, Canfield P C and Prozorov R 2013 *Phys. Rev. B* **88** 054514
- [61] Nakajima Y, Taen T, Tsuchiya Y, Tamegai T, Kitamura H and Murakami T 2010 *Phys. Rev. B* **82** 220504
- [62] Taen T, Ohtake F, Akiyama H, Inoue H, Sun Y, Pyon S, Tamegai T and Kitamura H 2013 *Phys. Rev. B* **88** 224514
- [63] Smylie M P et al 2016 *Phys. Rev. B* **93** 115119
- [64] Moroni M, Gozzelino L, Ghigo G, Tanatar M A, Prozorov R, Canfield P C and Carretta P 2017 *Phys. Rev. B* **96** 094523
- [65] Tarantini C et al 2010 *Phys. Rev. Lett.* **104** 087002
- [66] Yamakawa Y, Onari S and Kontani H 2013 *Phys. Rev. B* **87** 195121
- [67] Mott N 1929 *Proc. R. Soc. London A* **124** 425
- [68] Prozorov R, Kończykowski M, Tanatar M A, Thaler A, Bud'ko S L, Canfield P C, Mishra V and Hirschfeld P J 2014 *Phys. Rev. X* **4** 041032
- [69] Strehlow C P, Kończykowski M, Murphy J A, Teknowijoyo S, Cho K, Tanatar M A, Kobayashi T, Miyasaka S, Tajima S and Prozorov R 2014 *Phys. Rev. B* **90** 020508
- [70] Mishra V, Boyd G, Graser S, Maier T, Hirschfeld P J and Scalapino D J 2009 *Phys. Rev. B* **79** 094512
- [71] Hirschfeld P J and Goldenfeld N 1993 *Phys. Rev. B* **48** 4219
- [72] Bonn D A, Kamal S, Zhang K, Liang R, Baar D J, Klein E and Hardy W N 1994 *Phys. Rev. B* **50** 4051
- [73] Luetkens H et al 2008 *Phys. Rev. Lett.* **101** 097009
- [74] Williams T J et al 2010 *Phys. Rev. B* **82** 094512
- [75] Sonier J E et al 2011 *Phys. Rev. Lett.* **106** 127002
- [76] Valdés Aguilar R, Bilbro L S, Lee S, Bark C W, Jiang J, Weiss J D, Hellstrom E E, Larbalestier D C, Eom C B and Armitage N P 2010 *Phys. Rev. B* **82** 180514
- [77] Wu D, Barišić N, Dressel M, Cao G H, Xu Z A, Carbotte J P and Schachinger E 2010 *Phys. Rev. B* **82** 184527
- [78] Hashimoto K et al 2009 *Phys. Rev. Lett.* **102** 207001
- [79] Hashimoto K et al 2009 *Phys. Rev. Lett.* **102** 017002
- [80] Bobowski J S et al 2010 *Phys. Rev. B* **82** 094520
- [81] Yong J, Lee S, Jiang J, Bark C W, Weiss J D, Hellstrom E E, Larbalestier D C, Eom C B and Lemberger T R 2011 *Phys. Rev. B* **83** 104510
- [82] Luan L, Auslaender O M, Lippman T M, Hicks C W, Kalisky B, Chu J-H, Analytis J G, Fisher I R, Kirtley J R and Moler K A 2010 *Phys. Rev. B* **81** 100501
- [83] Luan L, Lippman T M, Hicks C W, Bert J A, Auslaender O M, Chu J-H, Analytis J G, Fisher I R and Moler K A 2011 *Phys. Rev. Lett.* **106** 067001
- [84] Prozorov R, Tanatar M A, Gordon R T, Martin C, Kim H, Kogan V G, Ni N, Tillman M E, Bud'ko S L and Canfield P C 2009 *Physica C* **469** 582
- [85] Song Y J, Ghim J S, Yoon J H, Lee K J, Jung M H, Ji H-S, Shim J H, Bang Y and Kwon Y S 2011 *Europhys. Lett.* **94** 57008
- [86] Okazaki R et al 2009 *Phys. Rev. B* **79** 064520
- [87] Klein T et al 2010 *Phys. Rev. B* **82** 184506
- [88] Joshi K R, Nusran N M, Cho K, Tanatar M A, Bud'ko S L, Canfield P C and Prozorov R in preparation
- [89] Shibauchi T, Hashimoto K, Okazaki R and Matsuda Y 2009 *Physica C* **469** 590
- [90] Malone L, Fletcher J D, Serafin A, Carrington A, Zhigadlo N D, Bukowski Z, Katrych S and Karpinski J 2009 *Phys. Rev. B* **79** 140501
- [91] Gordon R T, Martin C, Kim H, Ni N, Tanatar M A, Schmalian J, Mazin I I, Bud'ko S L, Canfield P C and Prozorov R 2009 *Phys. Rev. B* **79** 100506
- [92] Prozorov R and Kogan V G 2011 *Rep. Prog. Phys.* **74** 124505
- [93] Prozorov R and Giannetta R W 2006 *Supercond. Sci. Technol.* **19** R41
- [94] Prozorov R, Giannetta R W, Carrington A and Araujo-Moreira F M 2000 *Phys. Rev. B* **62** 115
- [95] Avci S et al 2012 *Phys. Rev. B* **85** 184507
- [96] Hashimoto K et al 2012 *Science* **336** 1554
- [97] Kim M G et al 2011 *Phys. Rev. B* **83** 054514
- [98] Kobayashi T, Miyasaka S, Tajima S and Chikumoto N 2014 *J. Phys. Soc. Japan* **83** 104702
- [99] Nandi S et al 2010 *Phys. Rev. Lett.* **104** 057006
- [100] Abdel-Hafiez M et al 2015 *Phys. Rev. B* **91** 024510
- [101] Mathur N D, Grosche F M, Julian S R, Walker I R, Freye D M, Haselwimmer R K W and Lonzarich G G 1998 *Nature* **394** 39
- [102] Tanatar M A et al 2014 *Phys. Rev. B* **89** 144514
- [103] Tanatar M A, Reid J-P, Shakeripour H, Luo X G, Doiron-Leyraud N, Ni N, Bud'ko S L, Canfield P C, Prozorov R and Taillefer L 2010 *Phys. Rev. Lett.* **104** 067002

- [104] Xu N *et al* 2013 *Phys. Rev. B* **88** 220508
- [105] Richard P, Qian T and Ding H 2015 *J. Phys.: Condens. Matter* **27** 293203
- [106] Tanatar M A, Torikachvili M S, Thaler A, Bud'ko S L, Canfield P C and Prozorov R 2014 *Phys. Rev. B* **90** 104518
- [107] Murphy J, Tanatar M A, Graf D, Brooks J S, Bud'ko S L, Canfield P C, Kogan V G and Prozorov R 2013 *Phys. Rev. B* **87** 094505
- [108] Luo X G *et al* 2009 *Phys. Rev. B* **80** 140503
- [109] Cho K, Kończykowski M, Murphy J, Kim H, Tanatar M A, Straszheim W E, Shen B, Wen H H and Prozorov R 2014 *Phys. Rev. B* **90** 104514
- [110] Evtushinsky D V *et al* 2009 *New J. Phys.* **11** 055069
- [111] Ding H *et al* 2008 *Europhys. Lett.* **83** 47001
- [112] Nakayama K *et al* 2011 *Phys. Rev. B* **83** 020501
- [113] Ota Y *et al* 2014 *Phys. Rev. B* **89** 081103
- [114] Reid J-P *et al* 2012 *Phys. Rev. Lett.* **109** 087001
- [115] Reid J-P *et al* 2012 *Supercond. Sci. Technol.* **25** 084013
- [116] Xiao-Chen H, Ai-Feng W, Zhen Z, Jian P, Lan-Po H, Xi-Gang L, Xian-Hui C and Shi-Yan L 2015 *Chin. Phys. Lett.* **32** 127403
- [117] Watanabe D *et al* 2014 *Phys. Rev. B* **89** 115112
- [118] Hashimoto K *et al* 2010 *Phys. Rev. B* **82** 014526
- [119] Maiti S, Sigrist M and Chubukov A 2015 *Phys. Rev. B* **91** 161102
- [120] Thomale R, Platt C, Hanke W, Hu J and Bernevig B A 2011 *Phys. Rev. Lett.* **107** 117001
- [121] Platt C, Thomale R, Honerkamp C, Zhang S-C and Hanke W 2012 *Phys. Rev. B* **85** 180502
- [122] Fernandes R M and Millis A J 2013 *Phys. Rev. Lett.* **111** 127001
- [123] Hardy F *et al* 2014 *J. Phys. Soc. Japan* **83** 014711
- [124] Hardy F *et al* 2016 *Phys. Rev. B* **94** 205113
- [125] Konczykowski M unpublished data
- [126] Kogan V G 2009 *Phys. Rev. B* **80** 214532
- [127] Almoalem A, Yagil A, Cho K, Teknowijoyo S, Tanatar M A, Prozorov R, Liu Y, Lograsso T A and Auslaender O M 2017 (arXiv:1708.00683)
- [128] Welp U, Xie R, Koshelev A E, Kwok W K, Luo H Q, Wang Z S, Mu G and Wen H H 2009 *Phys. Rev. B* **79** 094505
- [129] Li G, Hu W Z, Dong J, Li Z, Zheng P, Chen G F, Luo J L and Wang N L 2008 *Phys. Rev. Lett.* **101** 107004
- [130] Kim H *et al* 2014 *Phys. Rev. B* **90** 014517
- [131] Reid J-P *et al* 2016 *Phys. Rev. B* **93** 214519
- [132] Kasahara S *et al* 2010 *Phys. Rev. B* **81** 184519
- [133] Mizukami Y, Konczykowski M, Matsuura K, Watashige T, Kasahara S, Matsuda Y and Shibauchi T 2017 *J. Phys. Soc. Japan* **86** 083706
- [134] Lamhot Y, Yagil A, Shapira N, Kasahara S, Watashige T, Shibauchi T, Matsuda Y and Auslaender O M 2015 *Phys. Rev. B* **91** 060504
- [135] Rullier-Albenque F, Colson D, Forget A, Thuéry P and Poissonnet S 2010 *Phys. Rev. B* **81** 224503
- [136] Dhaka R S, Hahn S E, Razzoli E, Jiang R, Shi M, Harmon B N, Thaler A, Bud'ko S L, Canfield P C and Kaminski A 2013 *Phys. Rev. Lett.* **110** 067002
- [137] Thaler A, Ni N, Kracher A, Yan J Q, Bud'ko S L and Canfield P C 2010 *Phys. Rev. B* **82** 014534
- [138] Xu N *et al* 2012 *Phys. Rev. B* **86** 064505
- [139] Dulguun T, Mukuda H, Kobayashi T, Engetsu F, Kinouchi H, Yashima M, Kitaoka Y, Miyasaka S and Tajima S 2012 *Phys. Rev. B* **85** 144515
- [140] Murphy J, Strehlow C P, Cho K, Tanatar M A, Salovich N, Giannetta R W, Kobayashi T, Miyasaka S, Tajima S and Prozorov R 2013 *Phys. Rev. B* **87** 140505
- [141] van der Beek C J, Demirdis S, Colson D, Rullier-Albenque F, Fasano Y, Shibauchi T, Matsuda Y, Kasahara S, Gierlowski P and Konczykowski M 2013 *J. Phys.: Conf. Ser.* **449** 012023
- [142] Tanatar M A, Reid J-P, Shakeripour H, Luo X G, Doiron-Leyraud N, Ni N, Bud'ko S L, Canfield P C, Prozorov R and Taillefer L 2010 *Phys. Rev. Lett.* **104** 067002
- [143] Reid J-P, Tanatar M A, Luo X G, Shakeripour H, Doiron-Leyraud N, Ni N, Bud'ko S L, Canfield P C, Prozorov R and Taillefer L 2010 *Phys. Rev. B* **82** 064501
- [144] Li L J *et al* 2009 *New J. Phys.* **11** 025008
- [145] Sefat A S, Jin R, McGuire M A, Sales B C, Singh D J and Mandrus D 2008 *Phys. Rev. Lett.* **101** 117004
- [146] Lu X *et al* 2013 *Phys. Rev. Lett.* **110** 257001